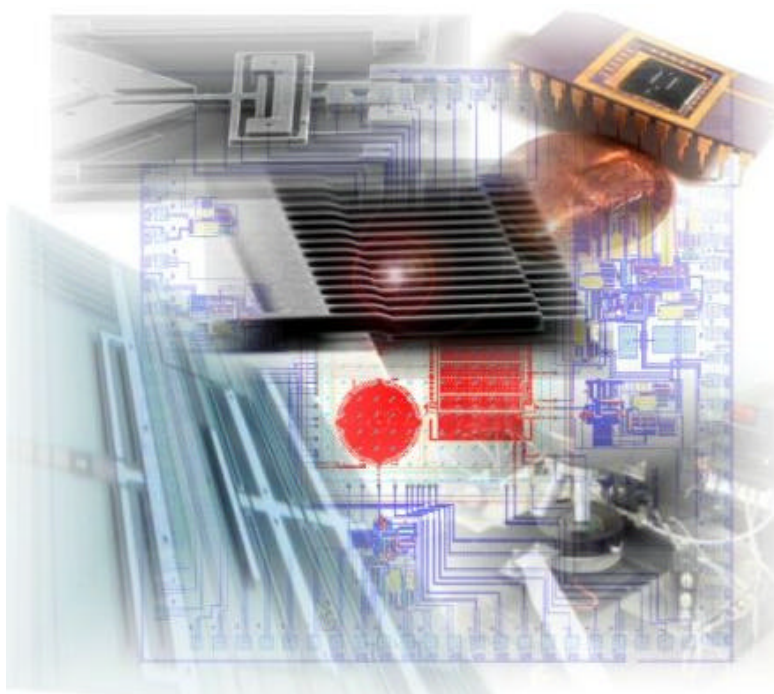


Four Degrees-of-Freedom Micromachined Gyroscope

Cenk Acar

23 October 2001
Technical Report No: MSL-01003



Contents

Contents	iv
List of Figures	v
Abstract of the Thesis	vi
1 Introduction	1
1.1 Micro-Electro-Mechanical Gyroscopes (MEMS Gyroscopes)	1
1.2 Conventional Micromachined Vibratory Rate Gyroscopes	2
1.2.1 Gyroscope Dynamics	2
1.2.2 Implementation	4
1.2.3 The Coriolis Effect	5
1.2.4 Conclusion	6
1.3 Problem Statement	6
1.4 Thesis Outline	7
2 A Novel Design Approach	8
2.1 Design Approach and Principle of Operation	8
2.1.1 The Design Basics	9
2.1.2 Principle of Operation	9
2.2 Gyroscope Dynamics	10
2.3 Summary	12
3 MEMS Implementation of the Design Concept	13
3.1 Mechanical Design	13
3.1.1 Suspension Design	13
3.1.2 Damping Estimation	15
3.2 Electrical Design	18
3.2.1 Electrostatic Actuation	19

3.2.2	Electrostatic Sensing	20
3.3	Dynamic Amplification in Drive Mode	21
3.4	Fabrication of a Prototype	23
3.4.1	MUMPs Surface Micromachining Process	24
3.4.2	Design Implementation Using MUMPs Technology	25
3.5	Conclusion	26
4	Parametric Sensitivity Analysis	30
4.1	Fabrication Variations	30
4.2	Pressure Fluctuations	30
4.3	Thermal Fluctuations	33
4.4	Residual Stresses	34
4.5	Conclusion	37
5	Conclusion and Future Work	38
5.1	Contribution	38
5.2	Future Work	39
5.2.1	Experimental Evaluation of the Prototype Designs	39
5.2.2	Control Issues	40
A	Gyroscope Simulation MATLAB Codes	45
A.1	gyroparameters.m	45
A.2	resonant freq.m	45
A.3	gyrodamping.m	46
A.4	electronic interface.m	46
A.5	single gyro two dof.m	46
A.6	dual drive oscillator.m	47
A.7	dual drive osc volt.m	48
A.8	full three dof ss.m	48
A.9	full three dof var.m	49
B	ANSYS Parametric Design Language (APDL) Codes	51
B.1	dualgyrofea.inp	51
B.2	singlegyrofea.inp	53

List of Figures

1.1	A conventional rate gyroscope has a single proof mass which is free to oscillate in two principle directions: drive and sense.	2
1.2	Time derivative of a vector in a rotating frame.	3
1.3	Schematic illustration of the inertial frame and the rotating gyroscope frame.	4
1.4	MEMS implementation of a conventional rate gyroscope.	5
1.5	The response of the system can be viewed as a 1-DOF system excited by the Coriolis force. Note that the gain is very sensitive to matching of drive and sense mode resonant frequencies, as well as damping fluctuations.	6
2.1	Lumped mass-spring-damper model of the dual-mass gyroscope. The first mass is driven in the x direction, and the response of the second mass along the y-axis is sensed.	8
2.2	Schematic illustration of a MEMS implementation of the dual-mass z-axis gyroscope.	9
2.3	Response of the dual-mass gyroscope in the flat operation region is insensitive to resonant frequency fluctuations and has over 15 times wider bandwidth than in conventional gyroscopes.	10
2.4	(a) Representation of the position vector of a body relative to the rotating frame. (b) Representation of the position vectors of the proof masses of the gyroscope relative to the rotating "gyroscope frame" B.	11
2.5	The 4-DOF dynamical system observed in the rotating gyroscope frame.	12
3.1	Illustration of the proposed dual-mass z-axis micromachined gyroscope design.	14
3.2	The fixed-guided end beam deflection.	14
3.3	Suspension system configuration provides two degrees of freedom (in drive and sense directions) for the active proof mass and the passive proof mass.	15
3.4	The first three resonant modes of the gyroscope. The simulation is performed using the finite element analysis package ANSYS. FEA results agree with the theoretical analysis within 0.1% error.	16

3.5	Illustration of Couette flow damping between two plates.	17
3.6	Illustration of Squeeze-film damping between two plates.	17
3.7	The capacitance between two plates.	18
3.8	(a) The comb-drive structure for electrostatic actuation. (b) The balanced comb-drive scheme.	19
3.9	The microscope photograph of the comb-drives attached to the first mass in the fabricated prototype z-axis dual-mass gyroscope.	20
3.10	The differential air-gap sense capacitors for response sensing.	20
3.11	Air-gap sense capacitors attached to the second mass in the fabricated prototype z-axis dual-mass gyroscope.	21
3.12	Lumped model of the drive mode of dual-mass gyroscope. The passive mass (m_2) amplifies the motion of the active mass (m_1).	21
3.13	(a) The magnitude plots of each proof mass. At the antiresonant frequency, which is the resonant frequency of the isolated passive mass-spring system, oscillation amplitude of the active mass approaches to zero. (b) The phase plots of the proof masses.	22
3.14	(a) The dynamic amplification ratio reaches its maximum at the antiresonant frequency, i.e., $\omega_{drive} = \sqrt{\frac{k_{2x}}{m_2}}$. (b) With a balanced interdigitated comb-drive scheme, a $1\mu m$ amplitude is achieved by the passive mass with a bias voltage of about 20V.	23
3.15	The fabrication steps of the three-layer MUMPs technology.	24
3.16	Cross-section of a device fabricated using the first two structural layers of MUMPs micromachining process [19].	25
3.17	Scanning Electron Microscope (SEM) photograph of the comb-drives.	26
3.18	Scanning Electron Microscope photograph of the air-gap capacitors.	26
3.19	The layout of the dual-mass z-axis gyroscope.	27
3.20	(a) The detailed view of the dual-mass z-axis gyroscope layout. (b) The Scanning Electron Microscope (SEM) photograph of the gyroscope prototype.	28
3.21	(a) The microscope photographs of the gyroscope prototype.	29
4.1	Fabrication variations can affect the geometry of the device by varying thickness of the structure or the width of the suspension beam elements. The proposed design illustrated in (b) is demonstrated to be more robust against these variations than the conventional approach illustrated in (a).	31

4.2	Change in the response due to: (a) $0.05\mu m$ variation in the width of suspension beams, (b) $0.1\mu m$ variation in thickness of the structure, (c) 10 GPa variation in Young's Modulus.	32
4.3	(a) Ambient pressure change from 100 millitorrs to 500 millitorrs results in 2% gain reduction for the proposed gyroscope design, (b) The same pressure change causes over 60% gain reduction for a conventional gyroscope design with similar geometry.	33
4.4	(a) Finite element simulation of the device with a uniform temperature loading of $100^{\circ}C$. Thermally induced localized stresses were observed only in the drive-direction beam elements of active mass, effecting only k_{1x} . (b) Static finite element analysis of the thermally loaded system with the modified Young's modulus. (c) Finite element analysis of a conventional gyroscope with similar geometry, under the same thermal loading. (d) Static analysis of the conventional design indicate the localized stresses leading to frequency mismatch between the drive and the sense resonant frequencies.	35
4.5	(a) Simulation of the proposed design's dynamical system with the perturbed parameters due to thermal loading was performed, indicating less than 0.9% gain deviation. (b) Simulation of the conventional design with the perturbed parameters indicates 7% gain error for the same thermal loading.	36
4.6	Effect of residual stresses (a) in x-direction, (b) in y-direction.	36
5.1	Experimental setup for experimental evaluation of prototype gyroscopes.	39
5.2	The implementation of the integrator for capacitive sensing.	40
5.3	Closed-loop driving scheme of the dual-mass gyroscope.	41
5.4	Modeling of anisoelectricity, the mis-alignment of the intended and the actual principle axes of oscillation.	42

ABSTRACT OF THE THESIS

Four Degrees-of-Freedom Micromachined Gyroscope

by

Cenk Acar

Master of Science in Mechanical and Aerospace Engineering

University of California, Irvine, 2001

Professor Andrei M. Shkel, Chair

In this thesis, a novel micromachined vibratory rate gyroscope design approach is presented. The device provides inherent robustness against fabrication variations, and fluctuations in the ambient temperature or pressure during the operation time of the device. With the new design concept, structural disturbance-rejection is achieved, shifting the complexity of the control electronics to complexity in the dynamical system. The thesis covers the operation principle of the design concept, followed by the detailed analysis of gyroscope dynamics. A MEMS implementation of this design concept is presented together with the details on the fabricated prototype devices. For demonstration of the improved robustness of the proposed system, the effects of realistic parameter variations on the system response are investigated, and the sensitivity of the proposed system to these variations is compared to the conventional design approach.

Chapter 1

Introduction

In this chapter, a general overview of conventional micromachined gyroscopes, and their operation principle is presented. Analysis of the dynamics, Coriolis response and implementation basics of the micromachined vibratory rate gyroscopes is followed by discussion of the limitations of the conventional approach, which defines the motivation of this thesis.

1.1 Micro-Electro-Mechanical Gyroscopes (MEMS Gyroscopes)

Even though there is an extensive variety of micromachined gyroscope designs and operation principles, almost all of the reported micromachined gyroscopes use vibrating mechanical elements to sense rotation. The vibrating mechanical elements have no rotating parts that require bearings, and hence they can be batch fabricated in micromachining processes. All vibratory gyroscopes are based on the transfer of energy between two vibration modes of a structure caused by Coriolis acceleration, which is induced due to an input rotation rate.

Micromachined gyroscopes for measuring rate or angle of rotation can be used in a wide spectrum of areas including automotive applications for ride stabilization and rollover detection; some consumer electronic applications, such as video-camera stabilization, virtual reality, and inertial mouse for computers, robotics applications, and a wide range of military applications; or to provide position information in inertial navigation systems together with micromachined accelerometers.

Precision fiber-optic gyroscopes, ring laser gyroscopes, and conventional rotating wheel gyroscopes are too expensive and too large for use in most emerging applications. With micromachining technologies, sensor size is reduced by orders of magnitude, and fabrication cost is dropped significantly. Moreover, advances in the fabrication techniques allow the electronics to be integrated on the same silicon chip together with the mechanical components.

1.2 Conventional Micromachined Vibratory Rate Gyroscopes

This section covers the basic operational principles of conventional micromachined vibratory rate gyroscopes. First, the dynamics of the vibratory gyroscopes is developed, then the MEMS implementation basics are presented. Also the response characteristics of the gyroscope to the rotation-induced Coriolis force is analyzed.

1.2.1 Gyroscope Dynamics

Almost all existing micromachined rate gyroscopes operate on the vibratory principle of a single proof mass suspended above the substrate. The proof mass is free to oscillate in two orthogonal directions (Fig. 1.1): the drive direction (x-Axis) and the sense direction (y-Axis) [1]. The overall dynamical system is simply a two degrees-of-freedom (2-DOF) mass-spring-damper system.

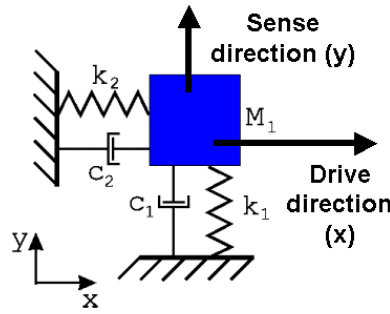


Figure 1.1: A conventional rate gyroscope has a single proof mass which is free to oscillate in two principle directions: drive and sense.

The principle of operation can be best understood by considering the rotation-induced Coriolis force acting on a body observed in a rotating reference frame. The accelerations experienced by a moving body in a rotating reference frame can be calculated having the following definitions:

FrameA : Inertial frame

FrameB : Rotating reference frame

\vec{r}_A : Position vector relative to inertial frame A

\vec{r}_B : Position vector relative to rotating frame B

$\vec{\theta}$: Orientation of rotating frame B

\vec{R} : Position of rotating frame B,

and the time derivative of a vector \vec{r} , which is defined in two reference frames A, and B as \vec{r}_A , and \vec{r}_B , respectively, is given as

$$\dot{\vec{r}}_A(t) = \dot{\vec{r}}_B(t) + \dot{\vec{\theta}} \times \vec{r}_B(t). \quad (1.1)$$

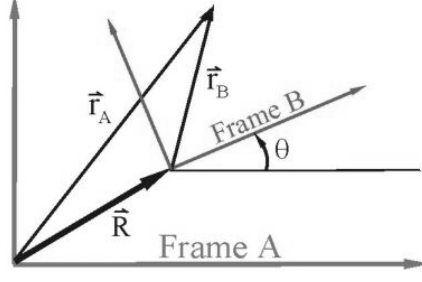


Figure 1.2: Time derivative of a vector in a rotating frame.

Taking the second time derivative of the position vector \vec{r} , the accelerations on a body moving with the rotating reference frame can be calculated as:

$$\vec{r}_A(t) = \vec{R}(t) + \vec{r}_B(t) \quad (1.2)$$

$$\dot{\vec{r}}_A(t) = \dot{\vec{R}}(t) + \dot{\vec{r}}_B(t) + \dot{\theta} \times \vec{r}_B(t) \quad (1.3)$$

$$\ddot{\vec{r}}_A(t) = \ddot{\vec{R}}(t) + \ddot{\vec{r}}_B(t) + \dot{\theta} \times \dot{\vec{r}}_B(t) + \dot{\theta} \times (\dot{\theta} \times \vec{r}_B(t)) + \ddot{\theta} \times \vec{r}_B(t) + \dot{\theta} \times \dot{\vec{r}}_B(t). \quad (1.4)$$

With the definition of \vec{v}_B and \vec{a}_B as the velocity and acceleration vectors with respect to the reference frame, \vec{a}_A as the acceleration vector with respect to the inertial frame, A as the linear acceleration of the reference frame, and $\vec{\Omega}$ as the angular velocity of the rotating frame; the expression for acceleration reduces to:

$$\vec{a}_A = A + \vec{a}_B + \vec{\Omega} \times \vec{r}_B + \vec{\Omega} \times (\vec{\Omega} \times \vec{r}_B) + 2\vec{\Omega} \times \vec{v}_B. \quad (1.5)$$

The last term $2\vec{\Omega} \times \vec{v}_B$ in the equation is called the Coriolis term. This acceleration term is of special interest since the rotation rate of the rotating reference frame B can be deduced by measuring the Coriolis acceleration. Consequently, the rate gyroscopes can be viewed as an accelerometer measuring the Coriolis acceleration to calculate the rotation rate.

When the acceleration vector of the proof mass is expressed with respect to the inertial frame by taking the second time derivative of the position vector (Figure 1.3), the equation of motion become

$$\vec{F}_{ext} = m(A + \vec{a}_B + \vec{\Omega} \times \vec{r}_B + \vec{\Omega} \times (\vec{\Omega} \times \vec{r}_B) + 2\vec{\Omega} \times \vec{v}_B) \quad (1.6)$$

where A is the linear acceleration and $\vec{\Omega}$ is the angular velocity of the rotating gyroscope frame, \vec{v}_B and \vec{a}_B are the velocity and acceleration vectors of the proof mass with respect to the reference frame, and \vec{F}_{ext} is the total external force applied to the proof mass.

If the motion is decomposed into the two principle oscillation directions, the drive and the sense directions, and if the linear accelerations are cancelled out by the control system, the two equations of motion can be expressed as

$$m\ddot{x} + c_x\dot{x} + (k_x - m(\Omega_y^2 + \Omega_z^2))x + m(\Omega_x\Omega_y - \dot{\Omega}_z)y = \tau_x + 2m\Omega_z\dot{y}$$

$$m\ddot{y} + c_y\dot{y} + (k_y - m(\Omega_x^2 + \Omega_z^2))y + m(\Omega_x\Omega_y + \dot{\Omega}_z)x = \tau_y - 2m\Omega_z\dot{x}. \quad (1.7)$$

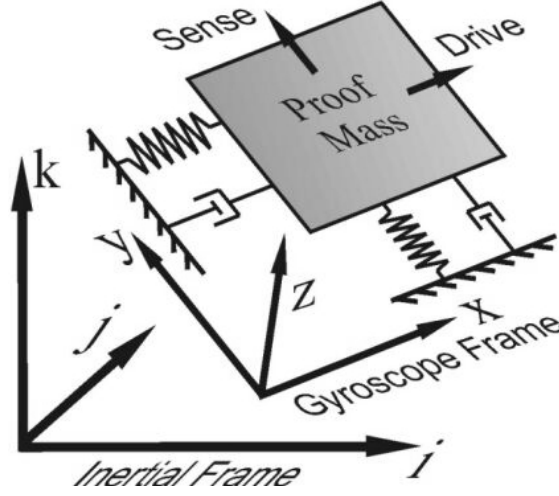


Figure 1.3: Schematic illustration of the inertial frame and the rotating gyroscope frame.

For a constant angular rate input $\dot{\Omega}_z = 0$, and for angular rates much lower than the driving frequency of the gyroscope, the terms Ω_x^2 , Ω_y^2 , and $\Omega_x\Omega_y$ can be neglected; resulting in the simplified 2-DOF equations of motion:

$$\begin{aligned} m\ddot{x} + c_x\dot{x} + k_x x &= \tau_x + 2m\Omega_z\dot{y} \\ m\ddot{y} + c_y\dot{y} + k_y y &= \tau_y - 2m\Omega_z\dot{x}. \end{aligned} \quad (1.8)$$

The two final terms $2m\Omega_z\dot{y}$, and $2m\Omega_z\dot{x}$ in the equation are the rotation-induced Coriolis forces, which cause dynamic coupling between the oscillation axes, and which are used for angular rate measurement.

1.2.2 Implementation

Most of the reported micromachined vibratory rate gyroscopes have a single proof mass suspended above the substrate. The proof mass is supported by anchored flexures, which serve as the flexible suspension between the proof mass and the substrate, making the mass free to oscillate in two orthogonal directions - the drive and the sense [1].

The proof mass is driven into resonance in the drive direction by an external sinusoidal force. The external force is generally the electrostatic forces applied by comb-drive structures (Figure 1.4), covered in Section 3.2.1. If the gyroscope is subjected to an angular rotation, the Coriolis force is induced in the y-direction. If the drive and sense resonant frequencies are matched, the Coriolis force excites the system into resonance in the sense direction. The resulting oscillation amplitude in the sense direction is proportional to the Coriolis force and, thus, to the angular velocity to be measured [3]. The sense direction oscillation is detected generally by air-gap capacitors (Figure 1.4), which is covered in Section 3.2.2, as well.

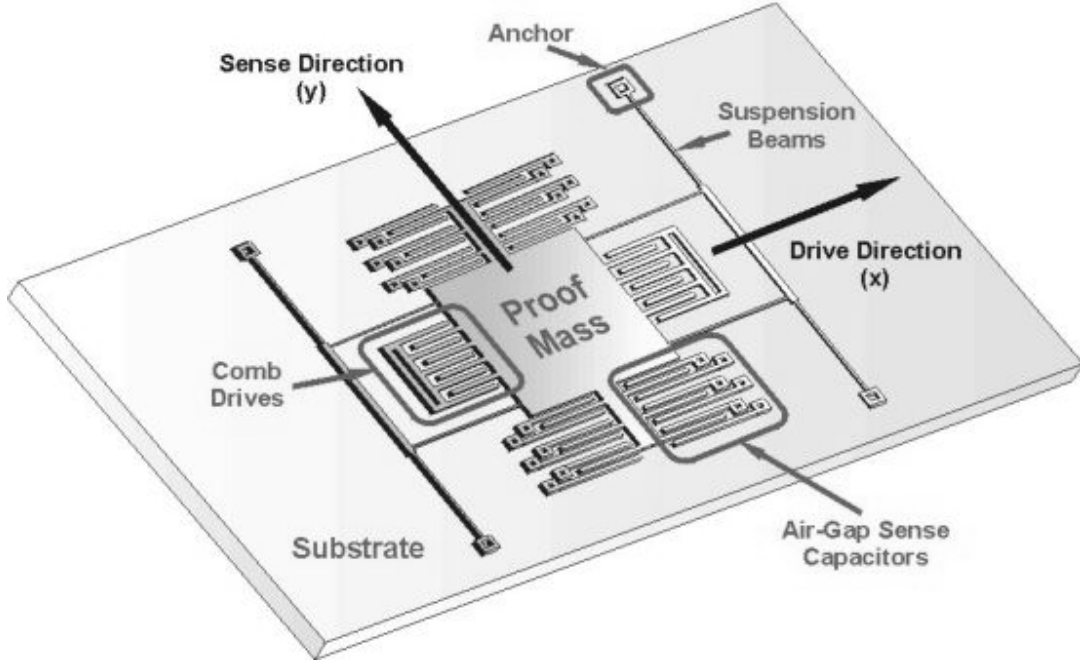


Figure 1.4: MEMS implementation of a conventional rate gyroscope.

1.2.3 The Coriolis Effect

To achieve the maximum possible gain, the conventional gyroscopes are generally designed to operate at or near the peak of the response curve. This is typically achieved by matching drive and sense resonant frequencies (Fig. 1.5). However, the system is very sensitive to variations in system parameters causing a shift in the resonant frequency.

Under high quality factor conditions the gain is high, however, the bandwidth is extremely narrow. For example, 1% fluctuation in frequency matching between drive and sense modes will produce an error of 20% in the output signal gain [4]. In addition, the gain is affected significantly by fluctuations in damping conditions (Figure 1.5).

Fabrication imperfections are inevitable, and affect material properties and geometry of MEMS structures. For surface micromachining, the thickness of the suspension elements is determined by deposition process, and the width is affected by etching process. In addition, Young's Modulus of the structure is affected by deposition conditions [2]. Variations in these parameters have drastic effect on dynamic response of gyroscopes. Generally, very sophisticated control electronics is used to provide operation in the region of the resonance peak [6]. Furthermore, during the operation time of these devices, fluctuations in the ambient temperature and pressure introduce significant errors (Figure 1.5).

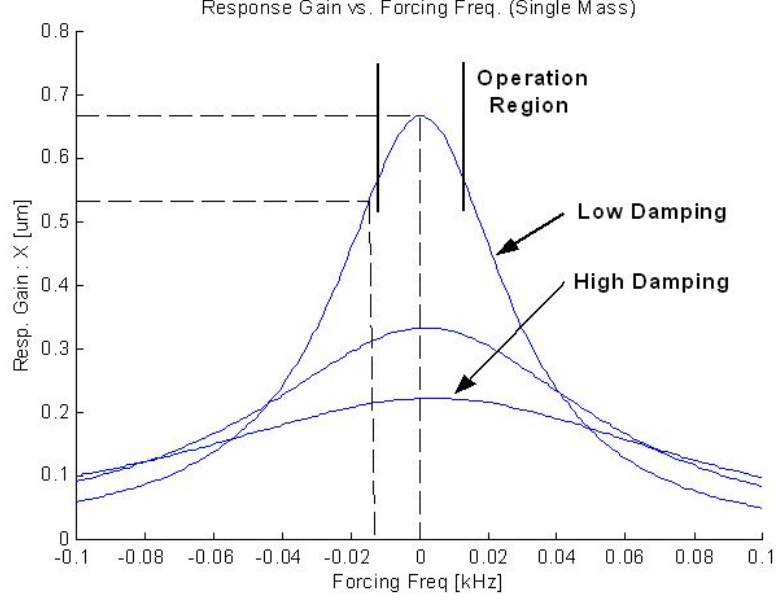


Figure 1.5: The response of the system can be viewed as a 1-DOF system excited by the Coriolis force. Note that the gain is very sensitive to matching of drive and sense mode resonant frequencies, as well as damping fluctuations.

1.2.4 Conclusion

In this section, the dynamics of a conventional vibratory rate gyroscope was developed, and the principle of operation of a MEMS implementation was discussed. It was concluded that the dynamic system response of the conventional single-mass gyroscope to the rotation-induced Coriolis force is very sensitive to variations in system parameters. Furthermore, the gain was observed to be affected significantly by fluctuations in damping conditions.

1.3 Problem Statement

The current state of the art micromachined gyroscopes require an order of magnitude improvement in performance, stability, and robustness. Fabrication variations and fluctuations in the ambient temperature or pressure during the operation time of these devices introduce significant errors, which have to be compensated by sophisticated control electronics. To eliminate the limitations of the existing micromachined gyroscopes, complexity of the control electronics can be shifted to complexity in the dynamical system. The objective of this thesis is to develop a new dynamical system design approach for gyroscopes, which will have inherent robustness against parameter variations, and require less active compensation.

1.4 Thesis Outline

This thesis covers a novel micromachined vibratory rate gyroscope design approach that provides inherent disturbance-rejection by the use of two independently oscillating proof masses. In Chapter 2, the operation principle of the design approach is discussed, and the dynamics of the 4-DOF system is analyzed. Chapter 3 covers the basics of the MEMS implementation of the design concept concentrating on the mechanical and electrical components of the system, along with the details on the fabricated prototype devices. In Chapter 4, the effects of realistic parameter variations on the system response are investigated, and the robustness of the proposed system against these variations is compared to the conventional designs. Finally, the conclusions and the future work are discussed in Chapter 5.

Chapter 2

A Novel Design Approach

In this chapter, a micromachined vibratory rate gyroscope design approach that suggests the use of two independently vibrating proof masses is presented. The principle of operation is also described. Finally, the dynamics of the 4-DOF system is derived and analyzed.

2.1 Design Approach and Principle of Operation

In contrast to the conventional micromachined gyroscopes, the proposed design approach utilizes a 4 degrees-of-freedom (DOF) dynamic system. In order to achieve dynamic amplification of mechanical motion, a system containing two vibrating proof masses (Fig. 2.2) is used. The increased degrees-of-freedom results in an increased design parameter space, which allows the dynamic response of the gyroscope to be shaped as needed with much less compromise in performance. An implementation of the conceptual design, Fig. 2.1, is illustrated in Fig. 2.2.

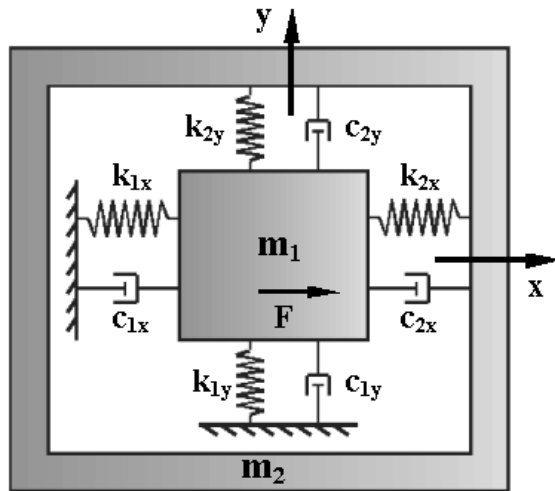


Figure 2.1: Lumped mass-spring-damper model of the dual-mass gyroscope. The first mass is driven in the x direction, and the response of the second mass along the y -axis is sensed.

2.1.1 The Design Basics

The dynamic system of the proposed micromachined gyroscope consists of the following main components: two vibrating proof masses suspended above the substrate, the flexures between the active mass and the ground that are anchored to the substrate, and the flexures between the active mass and the passive mass that mechanically couple both masses (Fig. 2.2).

The gyroscope has two orthogonal principle axes of oscillation: the drive direction (x-axis in Figure 2.1) and the sense direction (y-axis in Figure 2.1). Both of the proof masses are rendered free to oscillate in the drive and sense directions by the suspension system.

2.1.2 Principle of Operation

In the proposed design concept, the active mass (m_1 in Figure 2.1) is electrostatically forced to oscillate in the drive direction by the comb-drive structures built on each side of the mass (Fig. 2.2). There is no electrostatic force applied to the passive mass (m_2 in Figure 2.1), and the only forces acting on this mass are the elastic coupling forces and the damping forces. The design approach is based on dynamically amplifying the oscillation of the "active mass" by the "passive mass", as will be explained in Section 3.3. The response of the passive mass in the sense direction to the rotation-induced Coriolis force is monitored by the Air-Gap Sense Capacitors built around the passive mass (Fig. 2.2) providing the angular rate information.

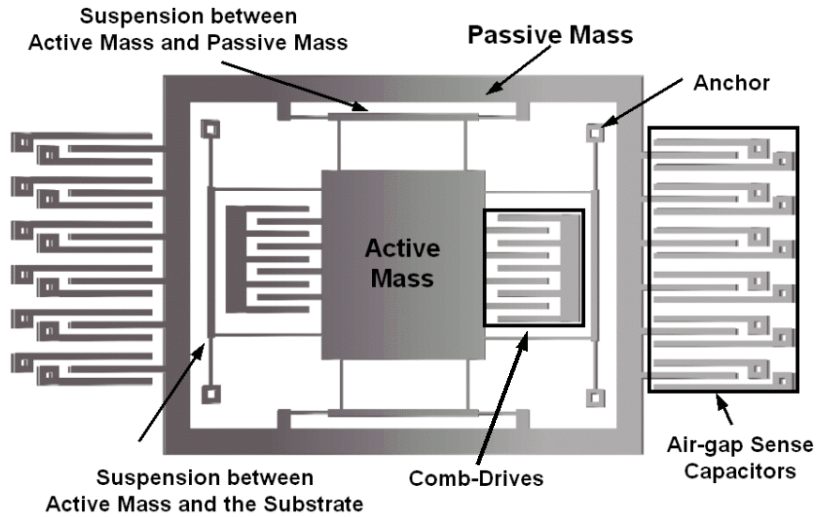


Figure 2.2: Schematic illustration of a MEMS implementation of the dual-mass z-axis gyroscope.

With appropriate selection of dynamical system parameters including the masses and the spring rates, the device will have the frequency response illustrated in Fig.2.3. There exists three regions of interest on this response curve: two resonant peaks, regions 1 and 3; and a flat region between the peaks, region 2. According to the proposed design approach, the nominal operation of the gyroscope is in the flat region, where the signal gain is relatively high, and

the sensitivity of the gain to driving frequency variations is low. Since the device is operated in the flat wide-bandwidth region, a 1% variation in natural frequencies of the system results in only 0.8% error in the output signal, whereas the same fluctuation will produce an error of 20% in the conventional micromachined gyroscopes [4].

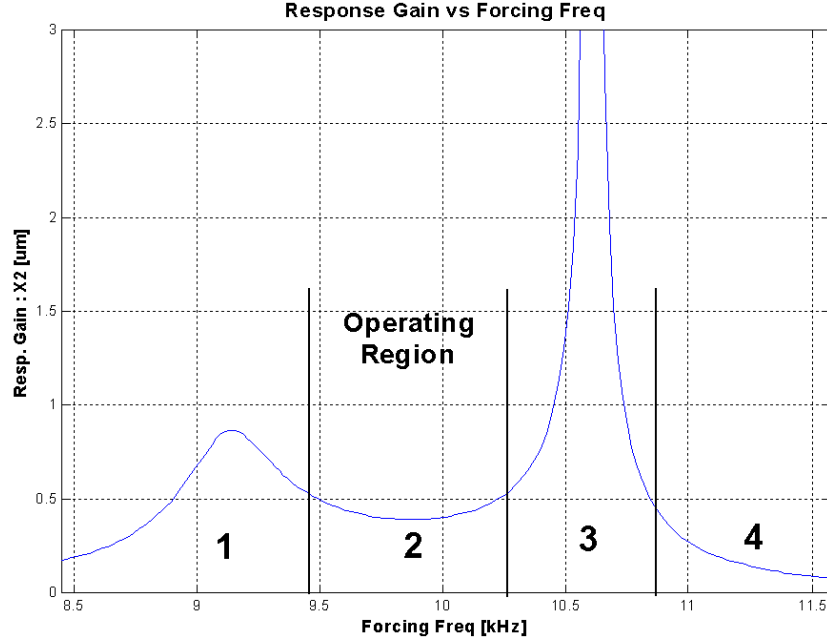


Figure 2.3: Response of the dual-mass gyroscope in the flat operation region is insensitive to resonant frequency fluctuations and has over 15 times wider bandwidth than in conventional gyroscopes.

2.2 Gyroscope Dynamics

The dynamics of the gyroscope should be considered in the non-inertial frame. Referring to Figure 2.4, the expression of absolute acceleration (in the inertial frame) of a rigid body with the position vector \vec{r} attached to a rotating reference frame B is

$$\vec{a}_A = \vec{a}_B + \vec{\Omega} \times \vec{r}_B + \vec{\Omega} \times (\vec{\Omega} \times \vec{r}_B) + 2\vec{\Omega} \times \vec{v}_B. \quad (2.1)$$

where the subscript A denotes "relative to inertial frame A", B denotes "relative to rotating gyroscope frame B", \vec{v}_B and \vec{a}_B are the velocity and acceleration vectors with respect to the reference frame respectively, $\vec{\Omega}$ is the angular velocity of the gyroscope frame, and the operation " \times " refers to cross-product of two vectors. The reference rotating gyroscope frame is assumed to be non-accelerating. The last term, $2\vec{\Omega} \times \vec{v}_B$, in the equation, the Coriolis term, is of special interest since the operation of the gyroscope depends on excitation of system in the sense direction by the Coriolis force due to this term. Thus, for a mass driven into oscillation in the x-direction, and subject to an angular rate Ω_z about the z-axis, the Coriolis acceleration induced in the y-direction reduces to

$$a_y = 2\Omega_z \dot{x}(t). \quad (2.2)$$

Similarly, when the active and passive masses are observed in the non-inertial rotating frame, the "gyroscope frame", additional inertial forces appear acting on both masses. The equations of motion for the two-mass system can be written as

$$\begin{aligned} m_1 \vec{a}_1 &= F_{2-1}^{\vec{}} + F_{s-1}^{\vec{}} - 2m_1 \vec{\Omega} \times \vec{v}_1 - m_1 \vec{\Omega} \times (\vec{\Omega} \times \vec{r}_1) - m_1 \dot{\vec{\Omega}} \times \vec{r}_1 \\ m_2 \vec{a}_2 &= F_{1-2}^{\vec{}} + F_{s-2}^{\vec{}} - 2m_2 \vec{\Omega} \times \vec{v}_2 - m_2 \vec{\Omega} \times (\vec{\Omega} \times \vec{r}_2) - m_2 \dot{\vec{\Omega}} \times \vec{r}_2 \end{aligned} \quad (2.3)$$

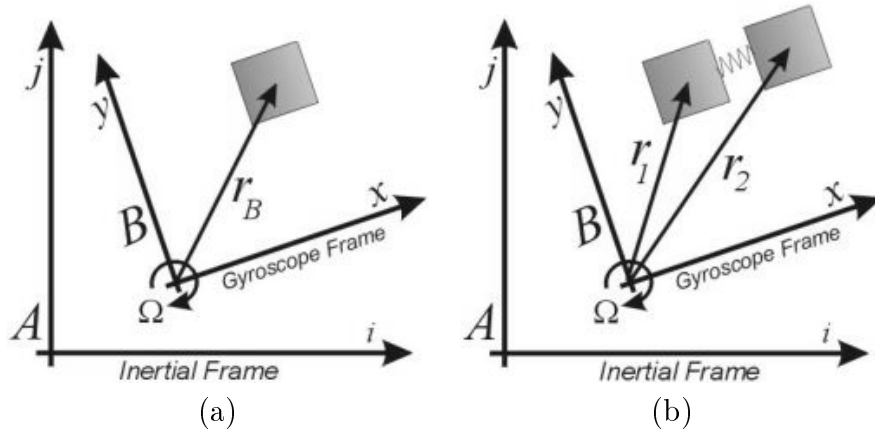


Figure 2.4: (a) Representation of the position vector of a body relative to the rotating frame. (b) Representation of the position vectors of the proof masses of the gyroscope relative to the rotating "gyroscope frame" B .

where \vec{r}_1 and \vec{r}_2 are the position vectors, \vec{v}_1 and \vec{v}_2 are the velocity vectors of the masses defined in the gyroscope frame, $F_{2-1}^{\vec{}}$ and $F_{1-2}^{\vec{}}$ are the opposing coupling forces between the masses that each mass applies on other depending on relative position $\vec{r}_2 - \vec{r}_1$, including spring and damping forces. $F_{s-1}^{\vec{}}$ consists of spring and damping forces between the active mass and the substrate, and $F_{s-2}^{\vec{}}$ includes the damping force between the passive mass and the substrate. Since both masses are subject to an angular rate of Ω_z about the axis normal to the plane of operation (z-axis), the equations of motion along the x-axis and y-axis become

$$\begin{aligned} m_1 \ddot{x}_1 + c_{1x} \dot{x}_1 + k_{1x} x_1 &= k_{2x} (x_2 - x_1) + c_{2x} (\dot{x}_2 - \dot{x}_1) + m_1 \Omega^2 x_1 - 2m_1 \Omega \dot{y}_1 + m_1 \dot{\Omega} y_1 + F_d(t) \\ m_2 \ddot{x}_2 + c_{2x} (\dot{x}_2 - \dot{x}_1) + k_{2x} (x_2 - x_1) &= m_2 \Omega^2 x_2 - 2m_2 \Omega \dot{y}_2 + m_2 \dot{\Omega} y_2 \\ m_1 \ddot{y}_1 + c_{1y} \dot{y}_1 + k_{1y} y_1 &= k_{2y} (y_2 - y_1) + c_{2y} (\dot{y}_2 - \dot{y}_1) + m_1 \Omega^2 y_1 + 2m_1 \Omega \dot{x}_1 + m_1 \dot{\Omega} x_1 \\ m_2 \ddot{y}_2 + c_{2y} (\dot{y}_2 - \dot{y}_1) + k_{2y} (y_2 - y_1) &= m_2 \Omega^2 y_2 + 2m_2 \Omega \dot{x}_2 + m_2 \dot{\Omega} x_2. \end{aligned} \quad (2.4)$$

where $F_d(t)$ is the driving electrostatic force applied to the active mass, and Ω is the angular velocity applied to the gyroscope about the z-axis.

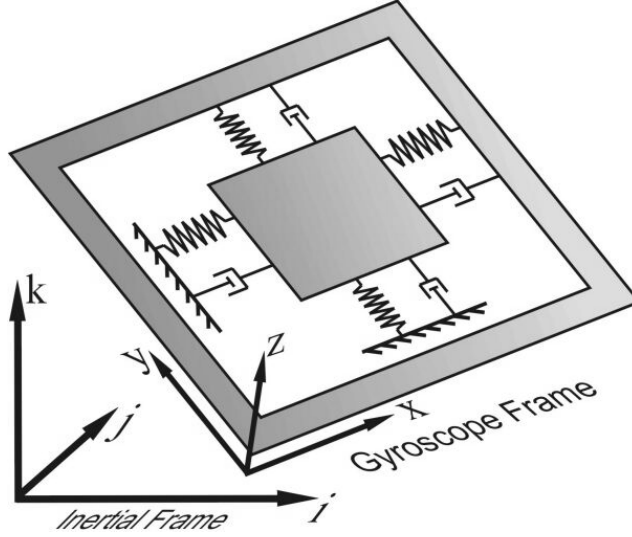


Figure 2.5: The 4-DOF dynamical system observed in the rotating gyroscope frame.

The overall dynamic model can be reduced having the active mass driven into forced oscillation in drive direction by $F_d(t)$ with a constant amplitude x_o and a frequency ω_d . Assuming the oscillation of the first mass in the drive direction is set by the control system to be

$$x_1 = x_o \cos(\omega_d t), \quad (2.5)$$

the system (2.4) reduces to three degrees of freedom. The equations of motion of the reduced system become [4]:

$$\begin{aligned} \ddot{y}_1 + 2\omega_n \xi \dot{y}_1 + 2\mu\omega_n \xi (y_1 - y_2) + (\omega_n - \Omega)y_1 + \omega_n^2 \sigma_1 (y_1 - y_2) &= -2\Omega\omega_d x_o \sin\omega_d t + \dot{\Omega}x_o \cos\omega_d t \\ \beta(\ddot{y}_2 - \Omega^2 y_2) + 2\mu\omega_n \xi (y_2 - y_1) - 2\beta\Omega\dot{x}_2 - \beta\dot{\omega}_z x_2 + \omega_n^2 \sigma_1 (y_2 - y_1) &= 0 \\ \beta(\ddot{x}_2 - \Omega^2 x_2) + 2\beta\Omega\dot{y}_2 + \beta\dot{\Omega}y_2 + \omega_n^2 \sigma_2 x_2 &= \omega_n^2 \sigma_2 x_o \cos\omega_d t \end{aligned} \quad (2.6)$$

where $\beta = m_2/m_1$, $\sigma_1 = k_{2y}/k_{1y}$, $\sigma_2 = k_{2x}/k_{1x}$, $\mu = c_2/c_1$, $\xi = c_1/(2m_1\omega_n)$, and ω_n is the natural frequency in the sense direction. Proper selection of system parameters will result in the frequency response illustrated in Figure 2.3.

2.3 Summary

The proposed vibratory rate gyroscope design approach was presented, and the principle of operation is described together with the detailed analysis of the 4-DOF system dynamics. With appropriate selection of dynamical system parameters, a flat region was observed in the response curve, where the sensitivity of the gain to driving frequency variations is low.

Chapter 3

MEMS Implementation of the Design Concept

This chapter describes the principle elements of a MEMS implementation of the conceptual design presented in Chapter 3. First, the suspension system and the damping components of the dynamic system are analyzed. Then, the basics of electrostatic actuation and capacitive sensing methods are presented, followed by a detailed analysis of the drive and sense components employed in the prototype design. Selection of design parameters for achieving dynamic amplification in the drive mode is addressed as well. In addition, fabrication of a prototype is discussed along with an overview of the used fabrication technology.

3.1 Mechanical Design

In this section, the main mechanical elements of the gyroscope design, including the suspension system and the damping components, are analyzed. The theoretical models of these components are also introduced.

3.1.1 Suspension Design

The complete suspension system of the device consists of two sets of four flexible beams per each mass. For each proof mass, one set of fixed-guided beams provides the desired spring rate in the drive direction, while the other set provides the desired spring rate in the sense direction (Figure 3.1). For a single fixed-guided beam (Figure 3.2), the translational stiffness for motion in the orthogonal direction to the beam axis is given by [12]

$$k_y = \frac{1}{2} \frac{3EI}{\frac{L^3}{2}} = \frac{Et w^3}{L^3}, \quad (3.1)$$

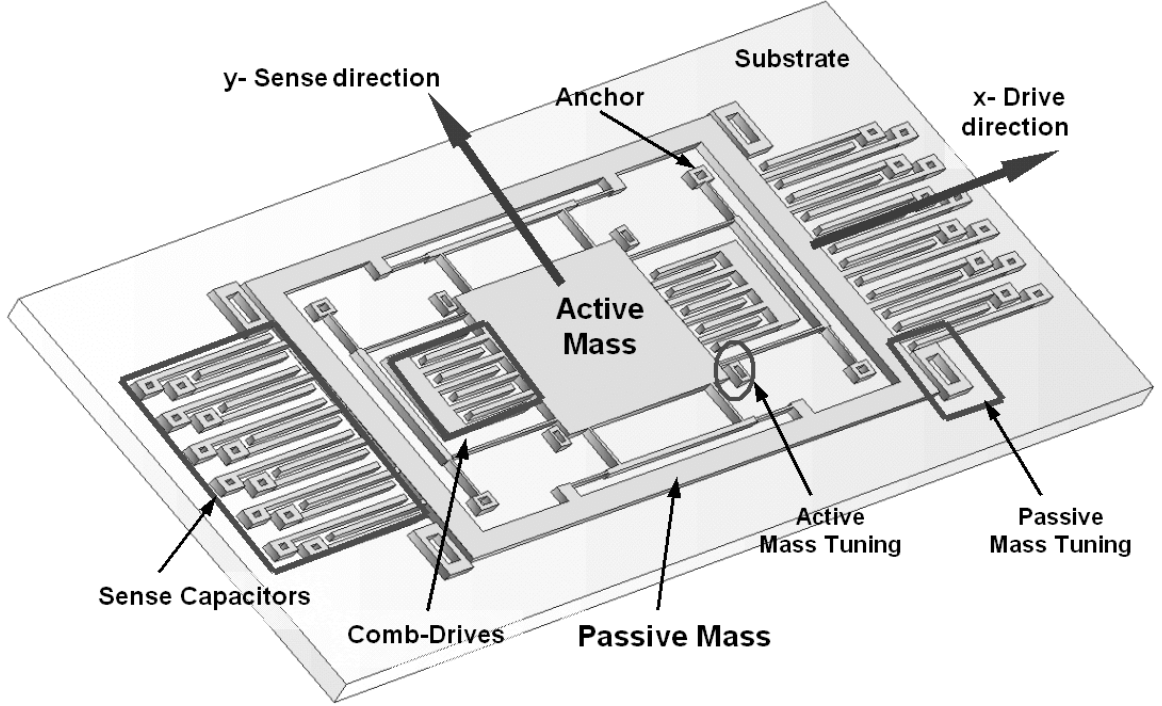


Figure 3.1: Illustration of the proposed dual-mass z-axis micromachined gyroscope design.

where E is the Young's Modulus, and I is the second moment of inertia. The beam length, thickness, and width are L , t , and w , respectively.

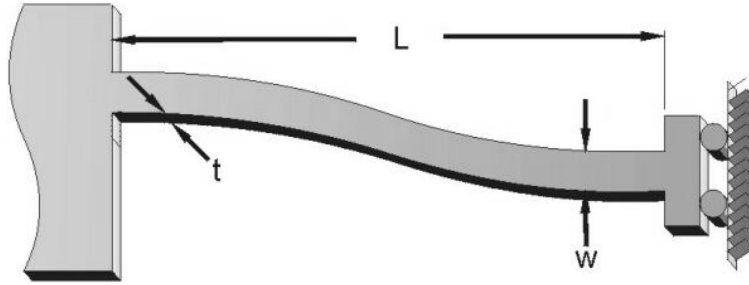


Figure 3.2: The fixed-guided end beam deflection.

Spring rates for a mass in drive or sense direction are determined by four fixed-guided beams if the axial strains in the other beams are neglected. This assumption is reasonable since the axial stiffness of a beam, $k_{axial} = \frac{Etw}{L}$, is generally four orders of magnitude ($\frac{L^2}{w^2}$ times) larger than the fixed-guided stiffness, which means the beams under axial load can be assumed infinitely stiff. Each stiffness value of the suspension can be calculated as

$$k_{1x} = \frac{4Etw^3}{L_{1x}^3}, k_{1y} = \frac{4Etw^3}{L_{1y}^3}, k_{2x} = \frac{4Etw^3}{L_{2x}^3}, k_{2y} = \frac{4Etw^3}{L_{2y}^3}. \quad (3.2)$$

where w and t are the width and thickness of the beam elements in the suspension, respectively. The individual beam lengths are shown in Figure 3.3. Finite element analysis of the gyroscope

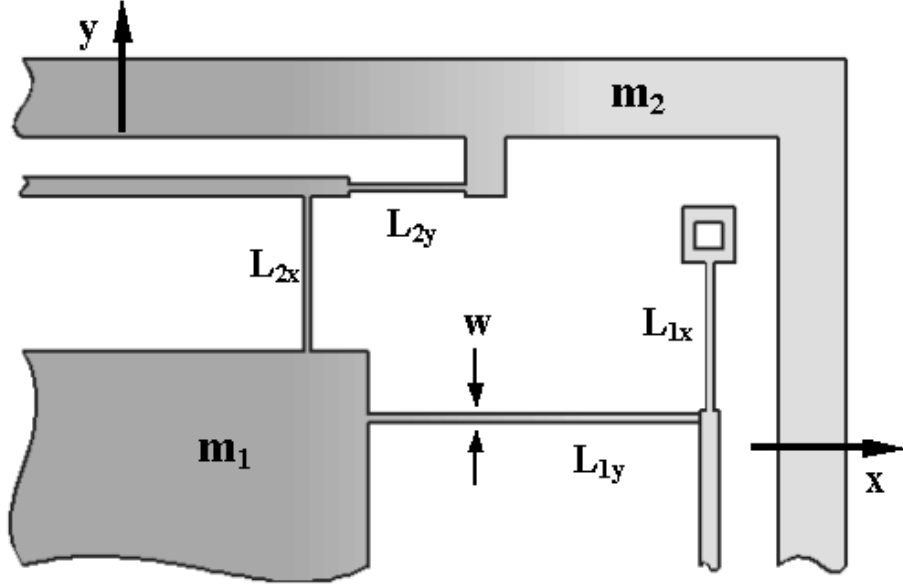


Figure 3.3: Suspension system configuration provides two degrees of freedom (in drive and sense directions) for the active proof mass and the passive proof mass.

is performed using the software package ANSYS to validate the assumptions in the theoretical analysis. The resonant frequencies obtained from the modal analysis matched the theoretically calculated parameters within 0.1% error. Furthermore, the unwanted resonant modes were observed to be over 4 kHz higher than the nominal operational frequency.

3.1.2 Damping Estimation

During the oscillation of the gyroscope proof masses, viscous effects of the air surrounding the structure results in damping. The structural damping of Polysilicon is orders of magnitude lower than the viscous damping, and is neglected in this analysis. The four damping coefficients (c_{1x} , c_{1y} , c_{2x} , and c_{2y}) in the dynamical system, shown in Figure 2.1, are due to the viscous effects of the air between the masses and the substrate, and in between the comb-drive and sense capacitor fingers. These viscous damping effects can be captured by using two general damping models: Couette flow damping and squeeze film damping.

Couette flow damping occurs when two plates of an area A , separated by a distance y_0 , slide parallel to each other (Figure 3.5). Assuming a Newtonian gas, the Couette flow damping coefficient can be approximated as:

$$c_{Couette} = \mu_p p \frac{A}{y_0}, \quad (3.3)$$

where $\mu_p = 3.710^{-4} \frac{kg}{m^2.s.torr}$ is the viscosity constant for air, p is the air pressure, A is the overlap area of the plates, y_0 is the plate separation.

Squeeze film damping occurs when two parallel plates approach each other and squeeze the

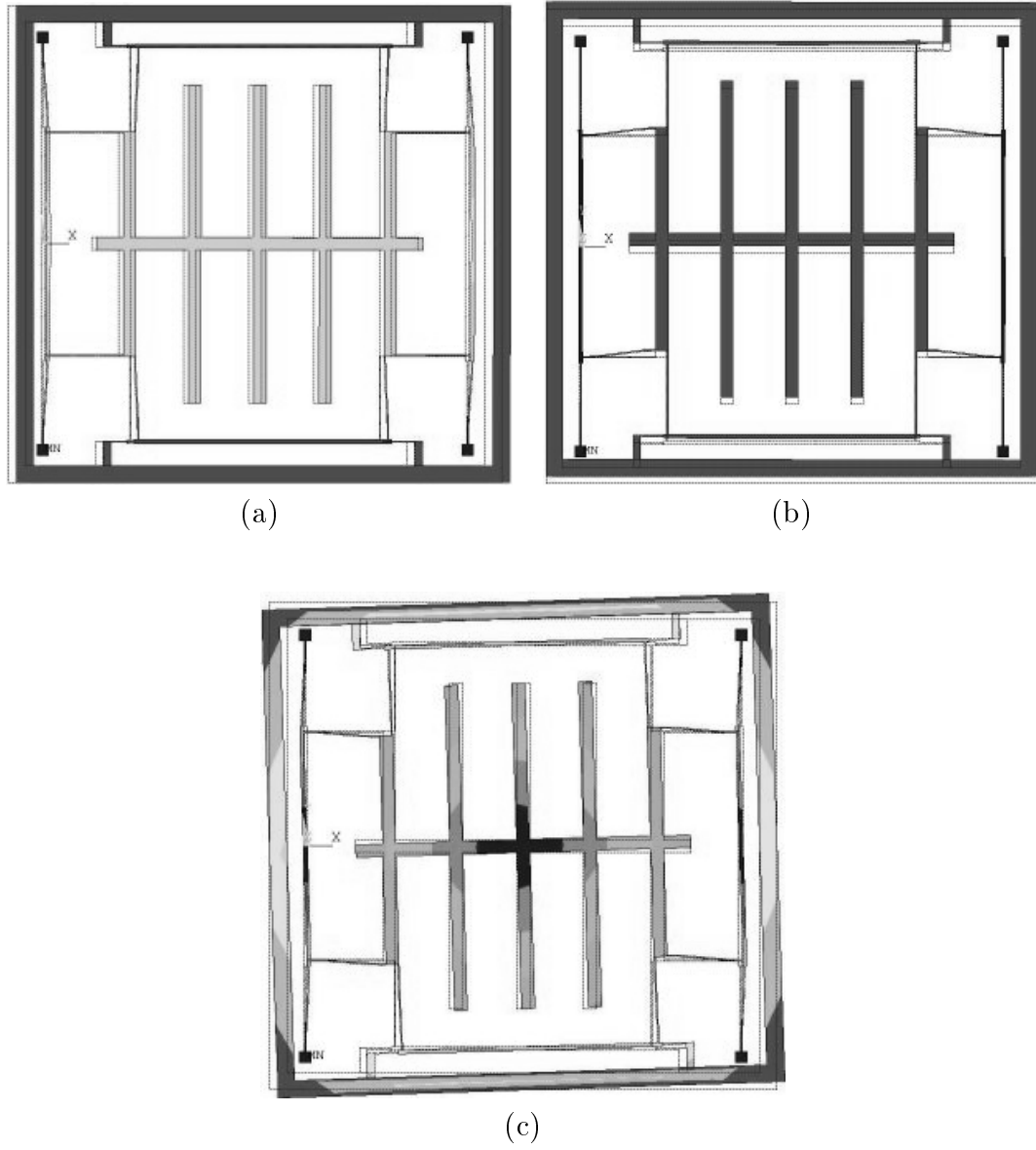


Figure 3.4: The first three resonant modes of the gyroscope. The simulation is performed using the finite element analysis package ANSYS. FEA results agree with the theoretical analysis within 0.1% error.

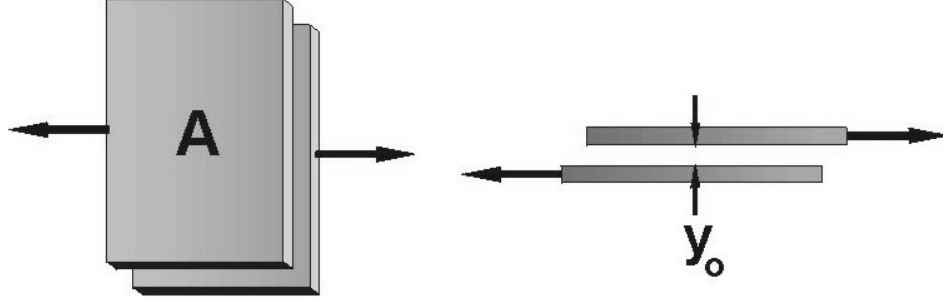


Figure 3.5: Illustration of Couette flow damping between two plates.

fluid film in between (Figure 3.6). Squeeze film damping effects are more complicated, and can exhibit both damping and stiffness effects depending on the compressibility of the fluid. Using the Hagen-Poiseuille law [2], squeeze film damping can be modeled as:

$$c_{Squeeze} = \mu_p p \frac{7A z_0^2}{y_0^3}. \quad (3.4)$$

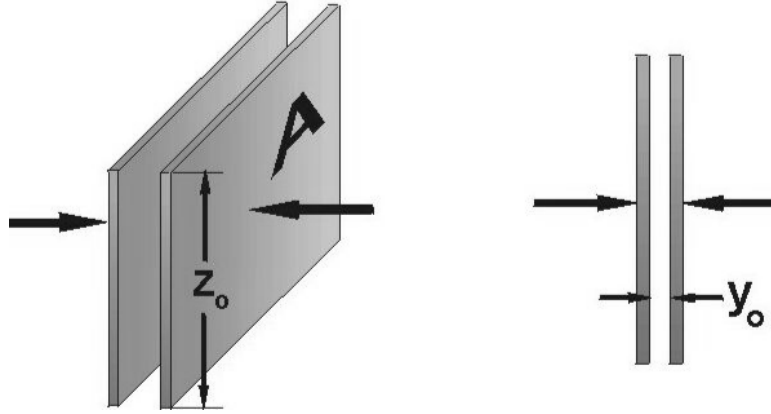


Figure 3.6: Illustration of Squeeze-film damping between two plates.

Utilizing the presented damping models; for the active mass, the total damping in the drive mode can be expressed as the sum of damping due to Couette flow between the mass and the substrate, and the damping due to Couette flow between the integrated comb fingers [2]:

$$c_{1x} = \mu_p p \frac{A_1}{z_0} + \mu_p p \frac{2N_{comb} l_{comb} t}{y_{comb}}, \quad (3.5)$$

where A_1 is the area of the active mass, z_0 is the elevation of the proof mass from the substrate, t is the thickness of the structure, N_{comb} is the number of comb-drive fingers, y_{comb} is the distance between the fingers, l_{comb} is the length of the fingers, p is the ambient pressure within the cavity of the packaged device, and $\mu_p = 3.710^{-4} \frac{kg}{m^2.s.torr}$ is the viscosity constant for air.

In the sense mode, the total damping is the sum of damping due to Couette flow between the proof mass and the substrate, and the Squeeze Film damping between the integrated comb fingers:

$$c_{1y} = \mu_p p \frac{A_1}{z_0} + \mu_p p \frac{7N_{comb}l_{comb}t^3}{y_{comb}^3}. \quad (3.6)$$

However, for the passive mass, the total damping in the drive mode results from Couette flow between the mass and the substrate, as well as Couette flow between the air-gap capacitor fingers:

$$c_{2x} = \mu_p p \frac{A_2}{z_0} + \mu_p p \frac{2N_{capacitor}l_{finger}t}{y_{capacitor}}, \quad (3.7)$$

where A_2 is the area of the passive mass, $N_{capacitor}$ is the number of air-gap capacitors, $y_{capacitor}$ is the distance between the capacitor fingers, and $l_{capacitor}$ is the length of the fingers.

Damping of the passive mass in the sense mode can be estimated as the combination of Couette flow between the proof mass and the substrate, and the Squeeze Film damping between the air-gap capacitor fingers:

$$c_{2y} = \mu_p p \frac{A_2}{z_0} + \mu_p p \frac{7N_{capacitor}l_{finger}t^3}{y_{capacitor}^3}. \quad (3.8)$$

These pressure dependent effective damping values will be used in the parametric sensitivity analysis simulations of the dynamic system.

3.2 Electrical Design

The micromachined gyroscope can be driven employing electrostatic forces, and the response can be sensed capacitively. Due to ease of manufacturing, electrostatic forcing and capacitive displacement sensing is preferred in most cases.

The electrostatic actuation and sensing components of the micromachined gyroscope can be modeled as a combination of parallel-plate capacitors (Figure 3.7). The capacitance between two parallel plates can be expressed as:

$$C = \frac{\varepsilon_0 A_{overlap}}{y_0} = \frac{\varepsilon_0 x_0 z_0}{y_0}. \quad (3.9)$$

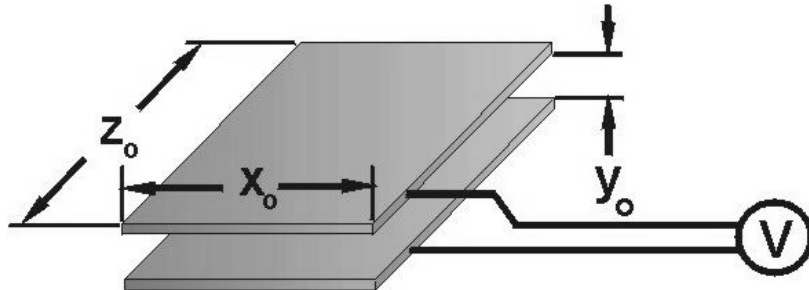


Figure 3.7: The capacitance between two plates.

The electrostatic force is generated due to the electrostatic conservative force field between the plates. Thus, the force can be expressed as the gradient of the potential energy U stored on the capacitor:

$$\vec{F} = -\nabla U = \frac{\nabla C(x, y, z)V^2}{2} = \frac{\varepsilon_0 \nabla \left(\frac{x_0 z_0}{y_0} \right) V^2}{2} \quad (3.10)$$

The electrostatic force generated in the x-direction as parallel plates slide over each other in the x-direction can be approximated as:

$$\vec{F}_x = \frac{\varepsilon_0 V^2 z_0}{2y_0}. \quad (3.11)$$

It should be noticed that this force is independent of x-direction displacement and the overlap area. However, the electrostatic force generated in the y-direction as the plates approach to each other in the y-direction depends on the overlap area, and is a nonlinear function of displacement:

$$\vec{F}_y = -\frac{\varepsilon_0 V^2 z_0 x_0}{2y_0^2}. \quad (3.12)$$

3.2.1 Electrostatic Actuation

Comb-drives are one of the most common actuation structures used in MEMS devices. The primary advantages of comb-drives (Figures 3.8a and 3.9) are the linearity of the generated forces, and the ability of applying displacement-independent forces.

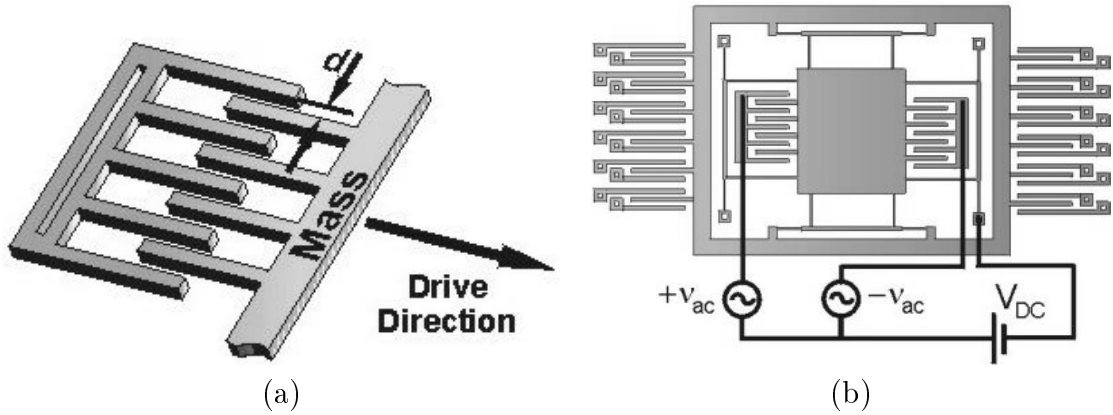


Figure 3.8: (a) The comb-drive structure for electrostatic actuation. (b) The balanced comb-drive scheme.

Linearized drive forces along the x-axis can be achieved by appropriate selection of voltages applied to the opposing comb-drive sets. A balanced interdigitated comb-drive scheme is imposed by applying $V_1 = V_{DC} + \nu_{AC}$ to one set of comb drives, and $V_2 = V_{DC} - \nu_{AC}$ to the other set (Figure 3.8b), where V_{DC} is a constant bias voltage, and ν_{AC} is a time-varying voltage [13]. Assuming negligible deflections along y-axis, the net electrostatic force reduces to

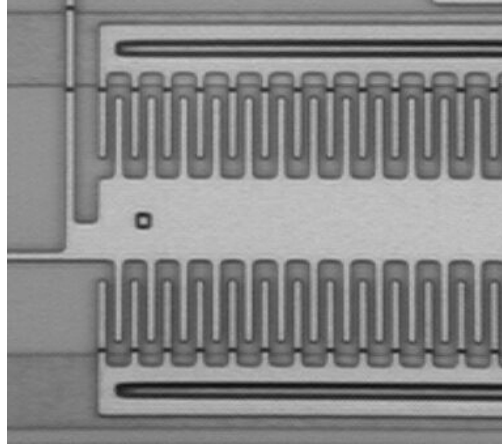


Figure 3.9: The microscope photograph of the comb-drives attached to the first mass in the fabricated prototype z-axis dual-mass gyroscope.

$$F = 4 \frac{\epsilon_0 z_0 N}{y_0} V_{DC} V_{AC}. \quad (3.13)$$

where z_0 is the finger thickness, and y_0 is the finger separation. It should be noticed that, the net force along the x-axis is independent of the displacement along the x-axis, and the overlap area of fingers.

3.2.2 Electrostatic Sensing

By building air-gap sense capacitors (Figures 3.10a and 3.11) around the second mass, the deflection can be capacitively sensed. When the second mass deflects in sense direction, the capacitance between the mass and the fixed electrodes changes.

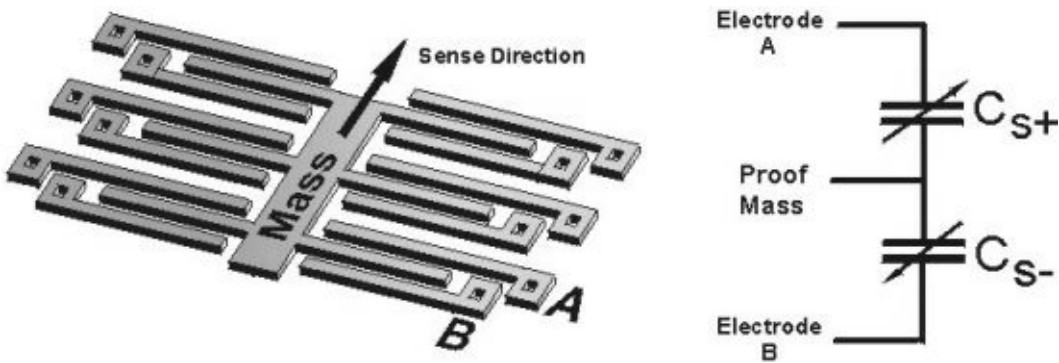


Figure 3.10: The differential air-gap sense capacitors for response sensing.

For a positive displacement, the finger attached to the mass (Figure 3.10) approaches finger A decreasing the capacitance C_{s+} , and moves away from finger B increasing the capacitance C_{s-} . The movement of the finger resulting from the deflection will translate the displacement

to a change in capacitance. Defining y_0 as the finger separation, l as the length of the fingers, and t as the thickness of the fingers; the differential capacitance values can be calculated as:

$$C_{s+} = C_{s-} = N \frac{\varepsilon_0 t l}{y_0}. \quad (3.14)$$

The capacitance change should be converted into a voltage signal. The purpose of the sense electronics is to detect the small capacitance changes resulting from very small displacements of the second mass, and to provide a sufficiently high sense voltage signal.

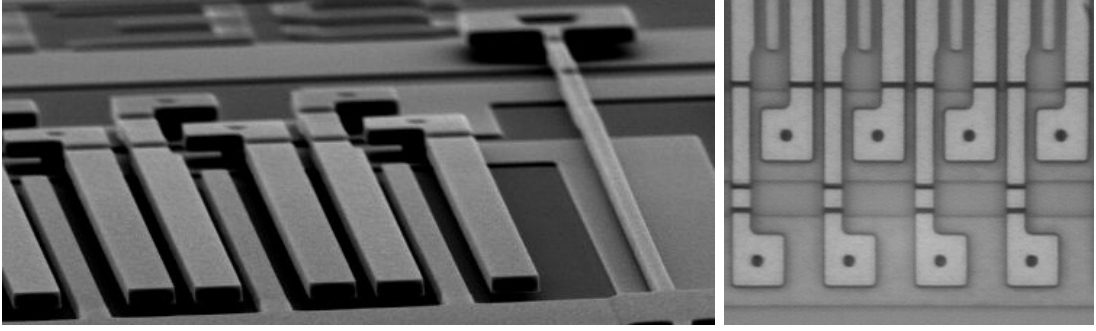


Figure 3.11: Air-gap sense capacitors attached to the second mass in the fabricated prototype z-axis dual-mass gyroscope.

3.3 Dynamic Amplification in Drive Mode

To achieve the maximum possible response of the gyroscope, amplitude of the drive-direction oscillation of the passive mass should be maximized. In the drive mode, the dynamic system is simply a 2-DOF system. A sinusoidal force is applied on the active mass by the comb-drive structure. Assuming a lumped parameter model, the equations of motion in the drive mode become:

$$\begin{aligned} m_1 \ddot{x}_1 + c_1 \dot{x}_1 + (k_1 + k_2)x_1 &= F + k_2 x_2 \\ m_2 \ddot{x}_2 + c_2 \dot{x}_2 + k_2 x_2 &= k_2 x_1. \end{aligned} \quad (3.15)$$

When a sinusoidal force $F = F_0 \sin(\omega t)$ is applied on the active mass by the interdigitated comb-drives, the steady-state response of the 2-DOF system will be

$$\begin{aligned} X_1 &= \frac{F_0}{k_1} \frac{1 - (\frac{\omega}{\omega_2})^2 + j\omega \frac{c_2}{k_2}}{[1 + \frac{k_2}{k_1} - (\frac{\omega}{\omega_1})^2 + j\omega \frac{c_1}{k_1}][1 - (\frac{\omega}{\omega_2})^2 + j\omega \frac{c_2}{k_2}] - \frac{k_2}{k_1}} \\ X_2 &= \frac{F_0}{k_1} \frac{1}{[1 + \frac{k_2}{k_1} - (\frac{\omega}{\omega_1})^2 + j\omega \frac{c_1}{k_1}][1 - (\frac{\omega}{\omega_2})^2 + j\omega \frac{c_2}{k_2}] - \frac{k_2}{k_1}}, \end{aligned} \quad (3.16)$$

where $\omega_1 = \sqrt{\frac{k_1}{m_1}}$ and $\omega_2 = \sqrt{\frac{k_2}{m_2}}$ are the resonant frequencies of the isolated active and passive mass-spring systems, respectively. When the driving frequency ω_{drive} is matched with the

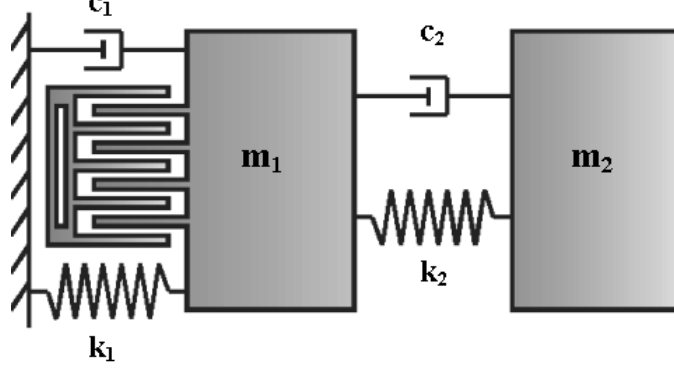


Figure 3.12: Lumped model of the drive mode of dual-mass gyroscope. The passive mass (m_2) amplifies the motion of the active mass (m_1).

resonant frequency of the isolated passive mass-spring system, i.e. $\omega_{drive} = \sqrt{\frac{k_{2x}}{m_2}}$, the passive mass moves to exactly cancel out the input force F applied to the active mass, and maximum dynamic amplification is achieved [9].

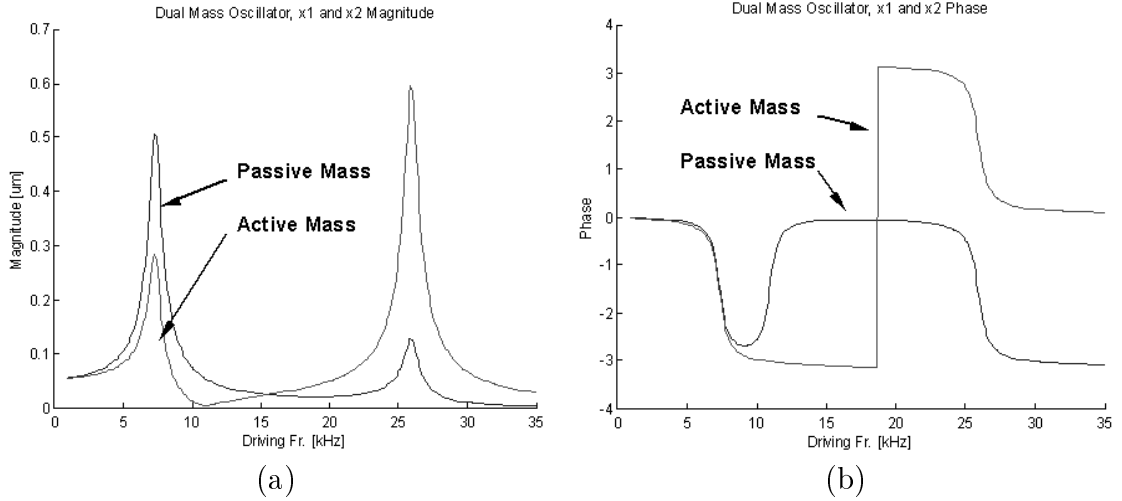


Figure 3.13: (a) The magnitude plots of each proof mass. At the antiresonant frequency, which is the resonant frequency of the isolated passive mass-spring system, oscillation amplitude of the active mass approaches to zero. (b) The phase plots of the proof masses.

The oscillation amplitudes in the drive-direction can be calculated once the magnitude of sinusoidal force $F = F_0 \sin(\omega t)$ applied to the active mass by the comb-drive structure is known. If a balanced interdigitated comb-drive scheme is utilized by applying $V_1 = V_{DC} + \nu_{AC}$ to one set of comb drives (e.g. the set on the right side in Fig. 2.2), and $V_2 = V_{DC} - \nu_{AC}$ to the opposing set (the set on the left side); the resulting net electrostatic force is linear in ν_{AC} , which will lead to simplification of the dynamic model:

$$F = 4 \frac{\epsilon_0 z_0 N}{y_0} V_{DC} \nu_{AC}, \quad (3.17)$$

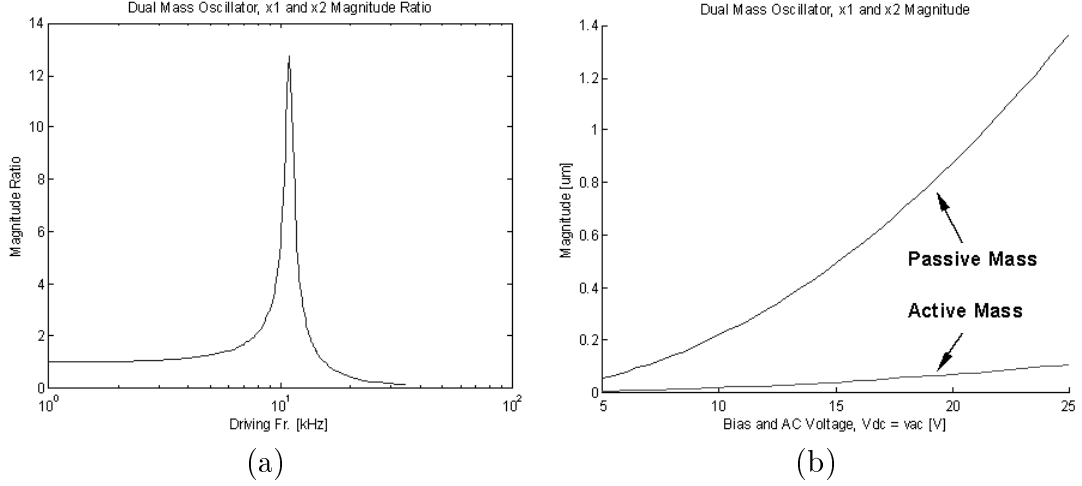


Figure 3.14: (a) The dynamic amplification ratio reaches its maximum at the antiresonant frequency, i.e., $\omega_{drive} = \sqrt{\frac{k_{2x}}{m_2}}$. (b) With a balanced interdigitated comb-drive scheme, a $1\mu m$ amplitude is achieved by the passive mass with a bias voltage of about 20V.

where $\nu_{AC} = |\nu_{AC}| \sin \omega t$ is the sinusoidal voltage, V_{DC} is the constant bias voltage, z_0 is the finger thickness, and y_0 is the finger separation. Thus, for the gyroscope, the magnitude of the applied drive force is simply

$$F_0 = 4 \frac{\varepsilon_0 z_0 N}{y_0} V_{DC} |\nu_{AC}|. \quad (3.18)$$

assuming small oscillation amplitudes of the active mass in the sense direction. With this balanced interdigitated comb-drive scheme, a $1\mu m$ oscillation amplitude is achieved by the passive mass in atmospheric pressure when a bias voltage of about 20V and a 5V alternating voltage is applied.

3.4 Fabrication of a Prototype

The design concept of a wide-bandwidth micromachined z-axis gyroscope can be implemented in any standard surface or bulk micromachining process. For the purpose of illustration, a design of a z-axis gyroscope implemented using two-layer $2\mu m$ surface micromachining fabrication process is presented.

The general features of a standard two-layer surface micromachining process include utilizing polysilicon as the structural material, LPCVD deposited oxide (PSG) as the sacrificial layer, and silicon nitride as electrical isolation between the polysilicon and the substrate.

In a standard three polysilicon layer surface micromachining process, the moving parts of the device are formed using the second structural polysilicon layer (Poly1) or the third (Poly2). The electrical connections are formed using the first structural polysilicon layer (Poly0) deposited on the nitride-covered substrate [19]. Summary of the process is followed.

3.4.1 MUMPs Surface Micromachining Process

For fabrication of a prototype of the gyroscope, commercially available Multi-User MEMS Processes (MUMPs) offered by Cronos/JDS Uniphase was used. MUMPs is a standard three-layer polysilicon surface micromachining technology. However, the prototype gyroscope structures employ only the first two structural layers, Poly0 and Poly1.

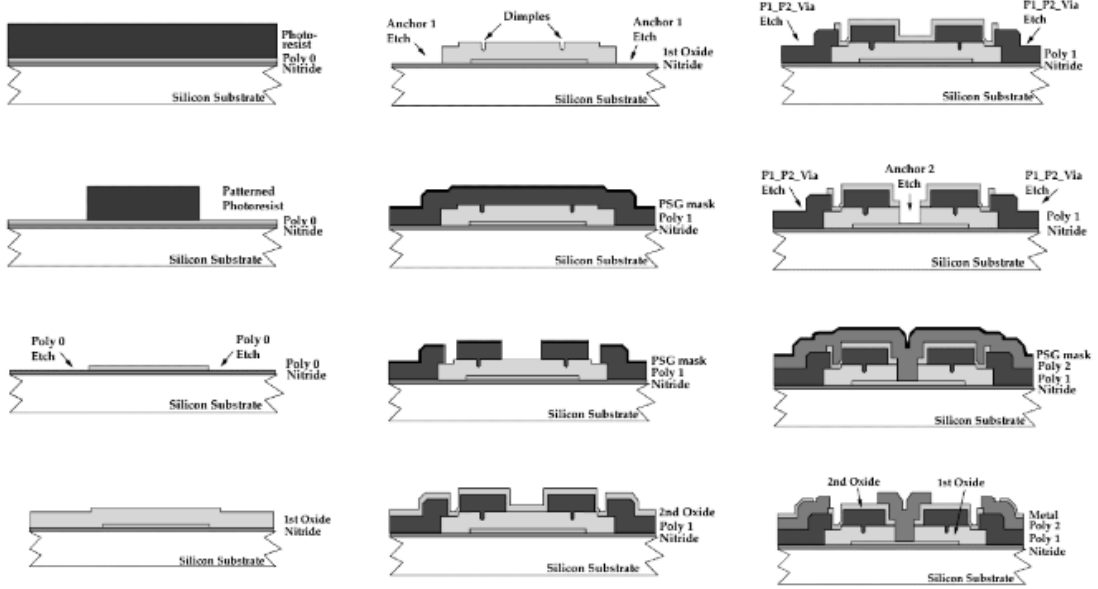


Figure 3.15: The fabrication steps of the three-layer MUMPs technology.

The first step of the fabrication process is deposition of a 600 *nm* low-stress Silicon Nitride layer on the silicon n-type (100) wafers as an electrical isolation layer. This is followed directly by the deposition of the first structural polysilicon film, Poly0, which is 500 *nm* thick. Poly0 is then photolithographically patterned: The Poly0 layer is first coated with photoresist. Then, photoresist is exposed with the first level mask (Poly0), and the exposed photoresist is developed to create the desired etch mask for subsequent pattern transfer to the underlying layer. After patterning the photoresist, the uncovered areas of the Poly0 layer is etched in an RIE (Reactive Ion Etch) system. The remaining photoresist is stripped away.

A 2.0 μm phosphosilicate glass (PSG) sacrificial layer is then deposited by LPCVD. This sacrificial layer of PSG, known as the Oxide layer, is removed at the end of the process to free the first mechanical layer of polysilicon. The sacrificial layer is lithographically patterned with the dimples mask and the dimples are transferred into the sacrificial PSG layer by RIE. The wafers are then patterned with the third mask layer, the anchor mask, and reactive ion etched. This step provides anchor holes that will be filled by the second polysilicon layer (Poly1). After etching anchors, the second structural layer of polysilicon is deposited. This structural layer has a thickness of 2.0 μm , and the moving structures including the proof mass, suspension system and the capacitors are formed in this layer. The polysilicon is

lithographically patterned using a mask designed to form the second structural layer POLY1. After etching the polysilicon, the photoresist is stripped.

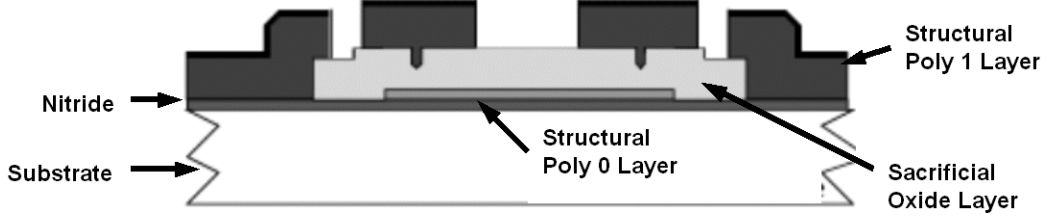


Figure 3.16: Cross-section of a device fabricated using the first two structural layers of MUMPs micromachining process [19].

The same procedure is followed to form the second sacrificial layer Oxide2 and the third structural layer Poly2. Throughout these steps, appropriate masks are used to form Anchor2 and Poly1-Poly2-Via structures. Finally, the wafer is diced, and the structures are released in HF Solution. Design rules to guarantee an error-free design, including minimum feature sizes, minimum gaps and etching hole specifications are available in the MUMPs Design Handbook by Cronos/JDS Uniphase [19].

3.4.2 Design Implementation Using MUMPs Technology

In the presented design, the proof masses and the flexures are formed in Poly1 with a $2\mu m$ thickness. The total footstep areas of the proof masses were calculated to achieve the required mass assuming a structural thickness of $2\mu m$ and a density of $2.33 \times 10^3 kg/m^3$:

$$m_2 = A_2 t \rho, \quad (3.19)$$

where A_1 and A_2 are the footstep areas of the masses m_1 and m_2 , respectively, t is the structural thickness, and ρ is the density of Polysilicon. Since the first sacrificial layer, Oxide1, has a thickness of $2\mu m$, the masses are suspended over the substrate with a $2\mu m$ clearance.

Interdigitated comb-drives structures which are used to drive the first mass into oscillations in the drive direction are formed in Poly1 (Figure 3.17).

The air-gap capacitors which are used to sense the response of the second mass in the sense direction are also formed in Poly1. The SEM photograph of the air-gap capacitor array built around the second mass is given in Figure 3.18. Parallel-plate capacitors are used to tune the response of the system, which are also formed in Poly1. The comb-drives, the air-gap capacitors, the parallel-plate capacitors, and the anchors grounding the proof masses are connected to the bonding-pads by connection lines formed in Poly0.

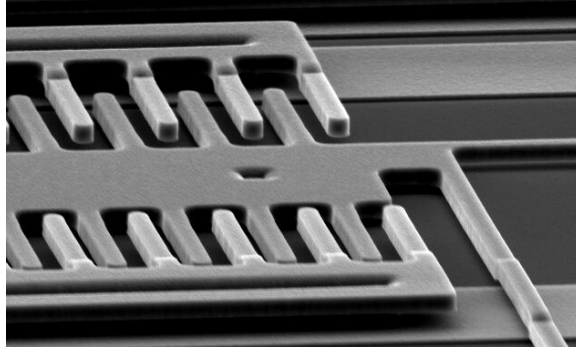


Figure 3.17: Scanning Electron Microscope (SEM) photograph of the comb-drives.

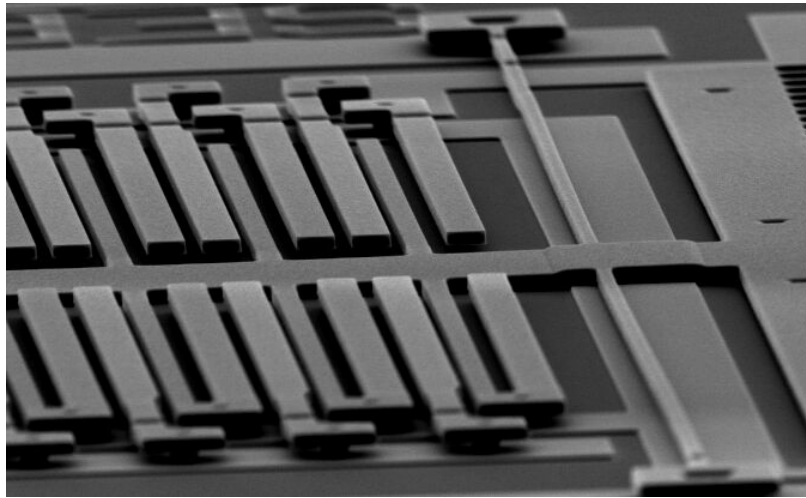


Figure 3.18: Scanning Electron Microscope photograph of the air-gap capacitors.

3.5 Conclusion

In this chapter, a MEMS implementation of the conceptual design was presented. The suspension system, damping effects, electrostatic actuation components, and capacitive sensing components were analyzed. The issue of achieving dynamic amplification in the drive mode was addressed, as well. Furthermore, MUMPs surface micromachining process, which was selected for fabrication of the prototypes was reviewed; and the design of the prototypes fabricated in the Cronos MUMPs 39 run was presented.

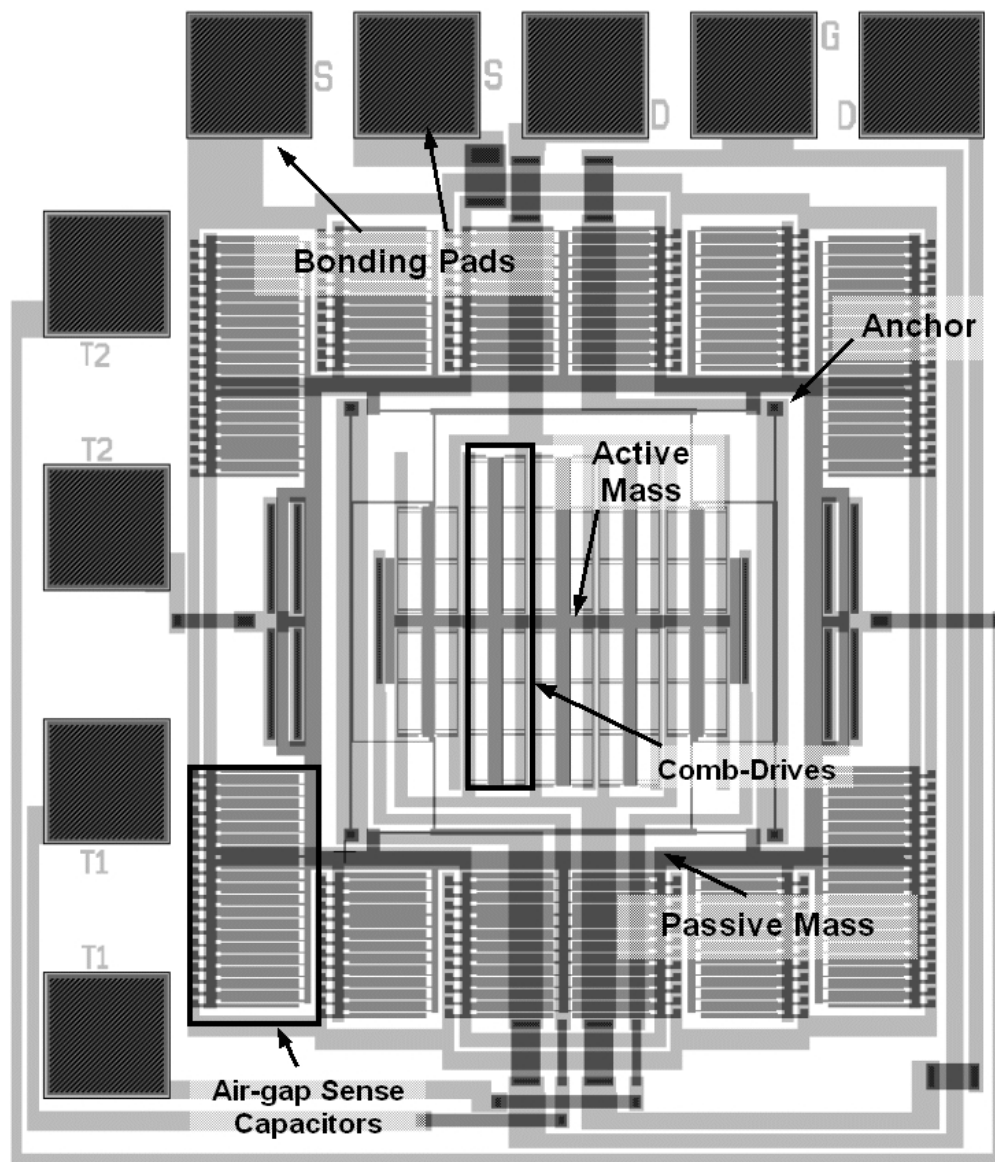


Figure 3.19: The layout of the dual-mass z-axis gyroscope.

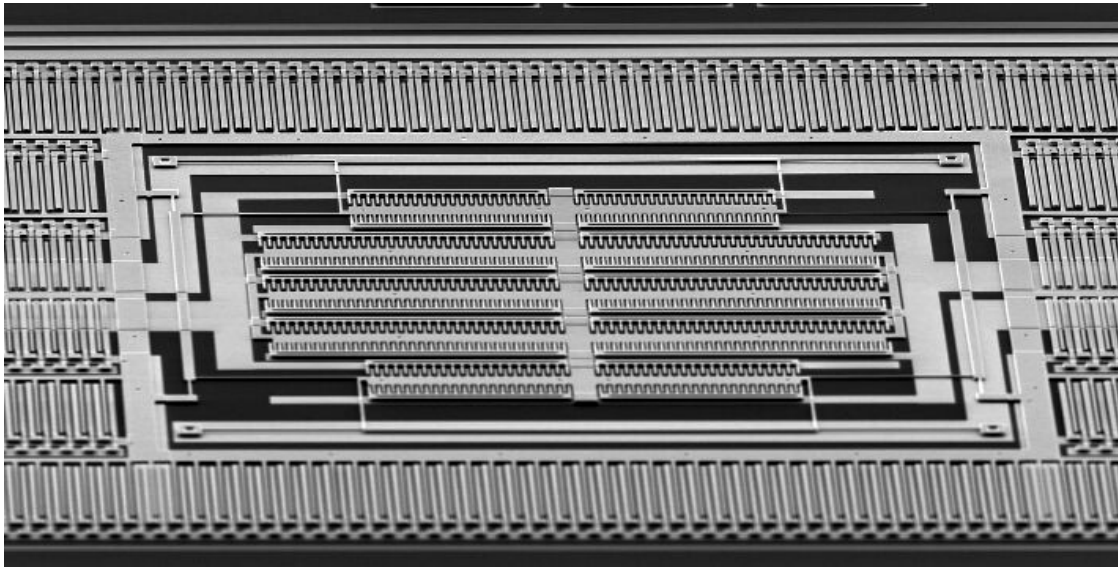
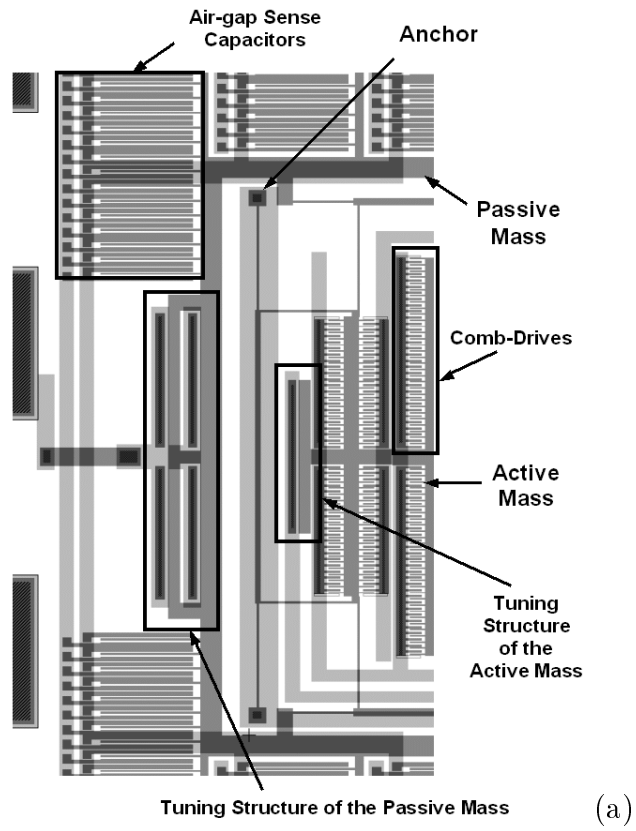


Figure 3.20: (a) The detailed view of the dual-mass z-axis gyroscope layout. (b) The Scanning Electron Microscope (SEM) photograph of the gyroscope prototype.

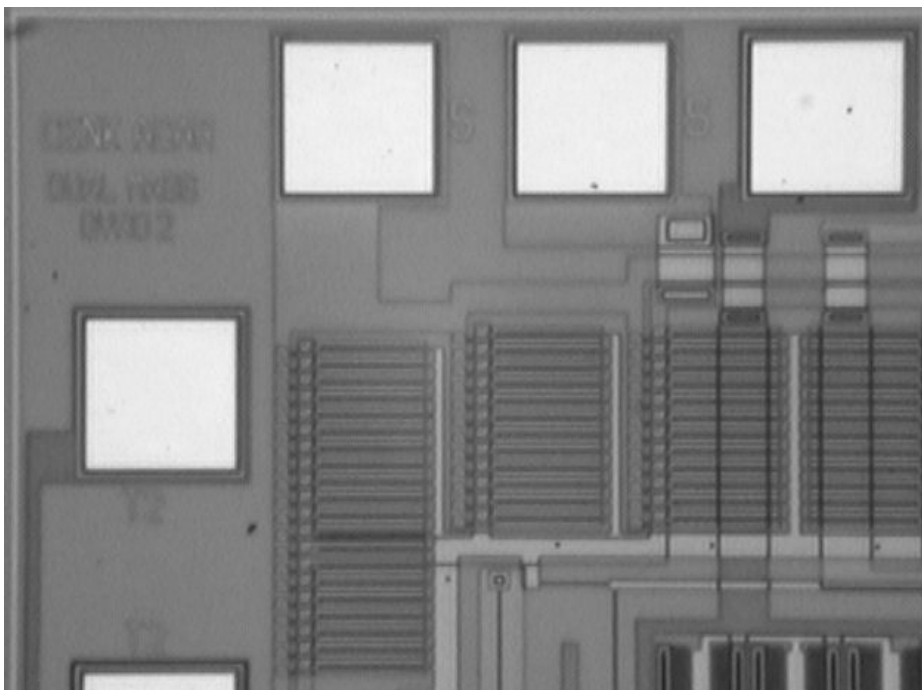
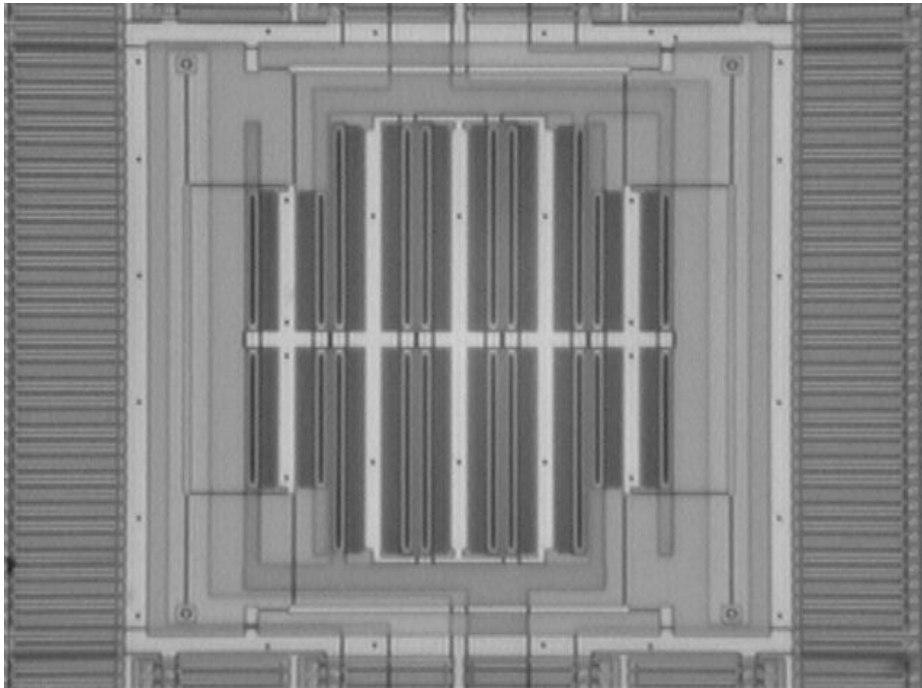


Figure 3.21: (a) The microscope photographs of the gyroscope prototype.

Chapter 4

Parametric Sensitivity Analysis

In this chapter, sensitivity analysis of the proposed micromachined gyroscope design is presented. Specifically, the sensitivity of the system response to realistic variations in system parameters, including fabrication, pressure, thermal, and residual stress effects, are investigated. In the analysis, the robustness of the proposed system against the parameter variations is compared to a conventional design with a similar geometry.

4.1 Fabrication Variations

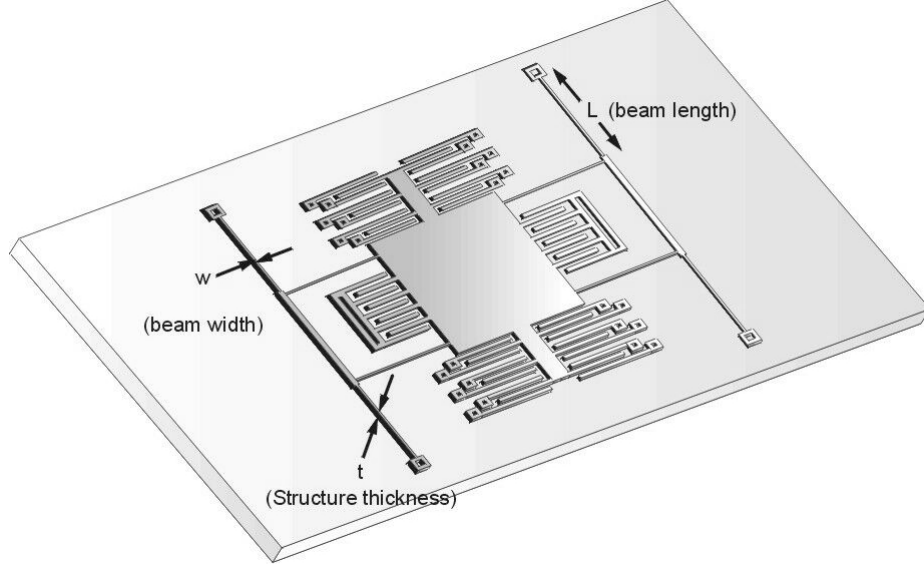
Fabrication variations affect the parameters of gyroscopes directly. For micromachining processes, the dimensions of the suspension beam elements are uncertain for different reasons. The length of the beams are determined solely by lithography, and are extremely accurate. However, the thickness is determined by deposition process, and the width set by lithography is affected by etching process. Thus, these parameters are less accurate, and can vary by 1% from wafer to wafer.

In conventional gyroscopes, fabrication variations result in resonant frequency shifts, requiring compensation by sophisticated control electronics. Yet, for the proposed system, a $0.05\ \mu\text{m}$ deviation from $2\ \mu\text{m}$ nominal beam width due to etching conditions results in less than 1% error in the gain (Fig. 4.3a). A $0.1\ \mu\text{m}$ deviation from $2\ \mu\text{m}$ nominal structure thickness due to deposition variations causes about 0.8% error in the gain (Fig. 4.3b).

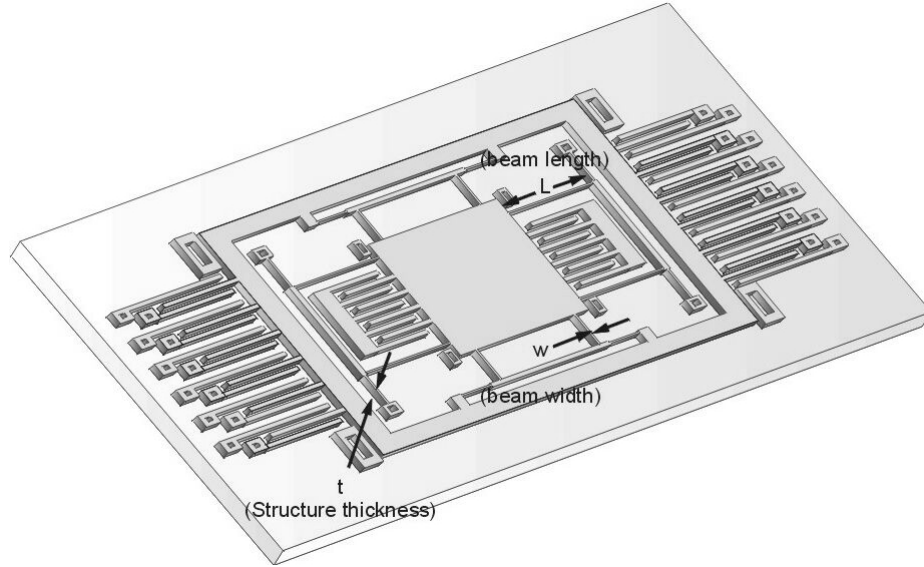
Moreover, a variation in deposition conditions that affect the Young's Modulus of the gyroscopes structure by 10 GPa causes less than 0.5% error in the gain (Fig. 4.3c). The same parameter variations in a conventional micromachined gyroscope without compensation by control electronics result in over 10% error.

4.2 Pressure Fluctuations

Pressure fluctuations can have significant effects on resonance dependent conventional gyroscopes. In contrast, since the proposed device utilizes dynamic amplification of mechanical

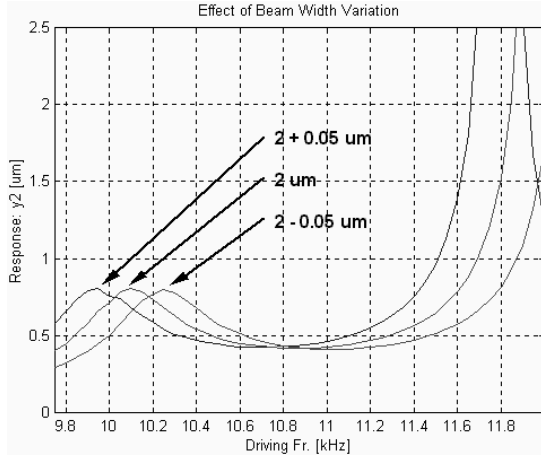


(a)

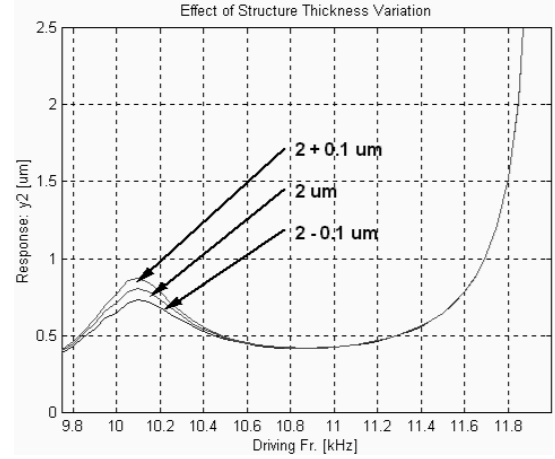


(b)

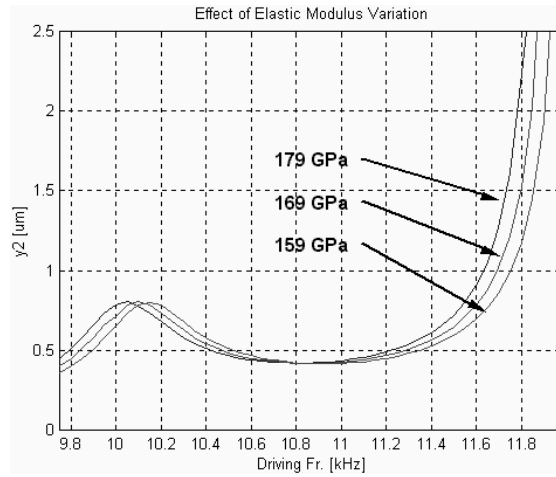
Figure 4.1: Fabrication variations can affect the geometry of the device by varying thickness of the structure or the width of the suspension beam elements. The proposed design illustrated in (b) is demonstrated to be more robust against these variations than the conventional approach illustrated in (a).



(a)



(b)



(c)

Figure 4.2: Change in the response due to: (a) $0.05 \mu\text{m}$ variation in the width of suspension beams, (b) $0.1 \mu\text{m}$ variation in thickness of the structure, (c) 10 GPa variation in Young's Modulus.

motion, and does not operate in resonance, the response is almost insensitive to damping changes in the operation region.

For a possible vacuum leakage from 100 millitorrs to 500 millitorrs, for example due to package sealing degradation over the operation time of the device, the response gain reduces by less than 2% (Fig. 4.3a). When the effect of same pressure variation on a conventional gyroscope design is analyzed, over 60% gain reduction is observed (Fig. 4.3b).

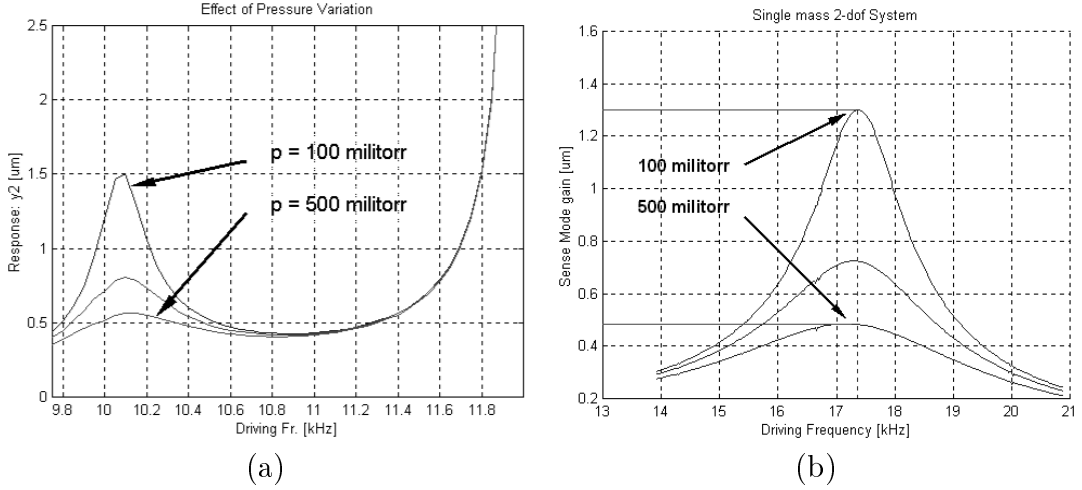


Figure 4.3: (a) Ambient pressure change from 100 millitorrs to 500 millitorrs results in 2% gain reduction for the proposed gyroscope design, (b) The same pressure change causes over 60% gain reduction for a conventional gyroscope design with similar geometry.

4.3 Thermal Fluctuations

Variations in the temperature of the structure can perturb the dynamical system parameters by three means: due to the inherent temperature dependence of Young's Modulus, due to changes in suspension geometry because of thermal expansion, and due to the thermally induced localized stress effects. Young's modulus of the structure at a given temperature can be calculated as [10]

$$E_{0^\circ C + \Delta T} = E_{0^\circ C} TC_E \Delta T + E_{0^\circ C}, \quad (4.1)$$

where $E_{0^\circ C}$ is the Young's modulus for fine-grained polysilicon at $0^\circ C$ (assumed 169 GPa), TC_E is the temperature coefficient of Young's modulus for polysilicon (assumed -75 ppm/ $^\circ C$ [10]), and ΔT is the temperature change. To reflect the effects of temperature dependent elastic modulus and thermal expansion on the resonant frequency of linear microresonators with folded-beam suspensions, the temperature coefficient of the resonance frequency can be determined as [10]

$$TC_f = \frac{1}{2}(TC_E - TC_h), \quad (4.2)$$

where TC_E is the temperature coefficient of the Young's modulus, and TC_h is the temperature coefficient of thermal expansion, which is assumed 2.5 ppm/ $^{\circ}\text{C}$; leading to a perturbed resonant frequency of

$$\omega_{n_{0^{\circ}\text{C}}+\Delta T} = \omega_{n_{0^{\circ}\text{C}}} TC_f \Delta T + \omega_{n_{0^{\circ}\text{C}}}. \quad (4.3)$$

However, for the proposed suspension system, more accurate results can be found conducting finite element analysis of the system. To be able to capture parameter changes due to the temperature dependence of Young's Modulus, due to thermal expansion generated alteration in suspension geometry, and due to thermally induced stresses; a finite element model of the device was created using the finite element analysis software package ANSYS. First, a uniform temperature loading of 100°C was applied to each surface, and the thermally induced localized stresses were observed. The results of the thermal finite element simulation indicated that a stress of 82 MPa was induced only in the drive-direction beam elements of active mass, effecting only k_{1x} . The other beam elements of the suspension system were observed stress-free (Figure 4.5a). Then, static structural analysis of the thermally loaded system with the modified Young's modulus was performed to calculate each of the four spring rates (k_{1x} , k_{1y} , k_{2x} , and k_{2y}) in the dynamical system shown in Figure 2.1. The same procedure was also carried out for a uniform temperature loading of -100°C . The simulation of the dynamical system with the perturbed parameters due to thermal loading indicated a deviation of less than 0.9% in the gain. Finite element analysis of a conventional gyroscope with similar geometry demonstrated about 7% gain error for the same thermal loading.

4.4 Residual Stresses

Accumulation of residual stresses in the structure directly affect the properties of the dynamical system. In the presence of residual stresses, the beam stiffness values, and thus the overall system spring rates change. Axial residual stresses in the x-direction effect only the y-direction spring rates (k_{1y} and k_{2y}) of the suspension, while axial residual stresses in y direction effect only the x-direction spring rates (k_{1x} and k_{2x}).

Thus, for the suspension system with an x-direction axial residual stress of ε_x and a y-direction axial residual stress of ε_y , the spring rate values become [3]

$$k_{1x} = \frac{Etw\kappa_y^2}{12L_{1x}} \left[1 - \frac{2w}{\beta_{1x}L_{1x}} \frac{\cosh(\frac{\kappa_y L_{1x}}{w}) - 1}{\sinh(\frac{\kappa_y L_{1x}}{w})} \right]^{-1} \quad (4.4)$$

$$k_{1y} = \frac{Etw\kappa_x^2}{12L_{1y}} \left[1 - \frac{2w}{\beta_{1y}L_{1y}} \frac{\cosh(\frac{\kappa_x L_{1y}}{w}) - 1}{\sinh(\frac{\kappa_x L_{1y}}{w})} \right]^{-1} \quad (4.5)$$

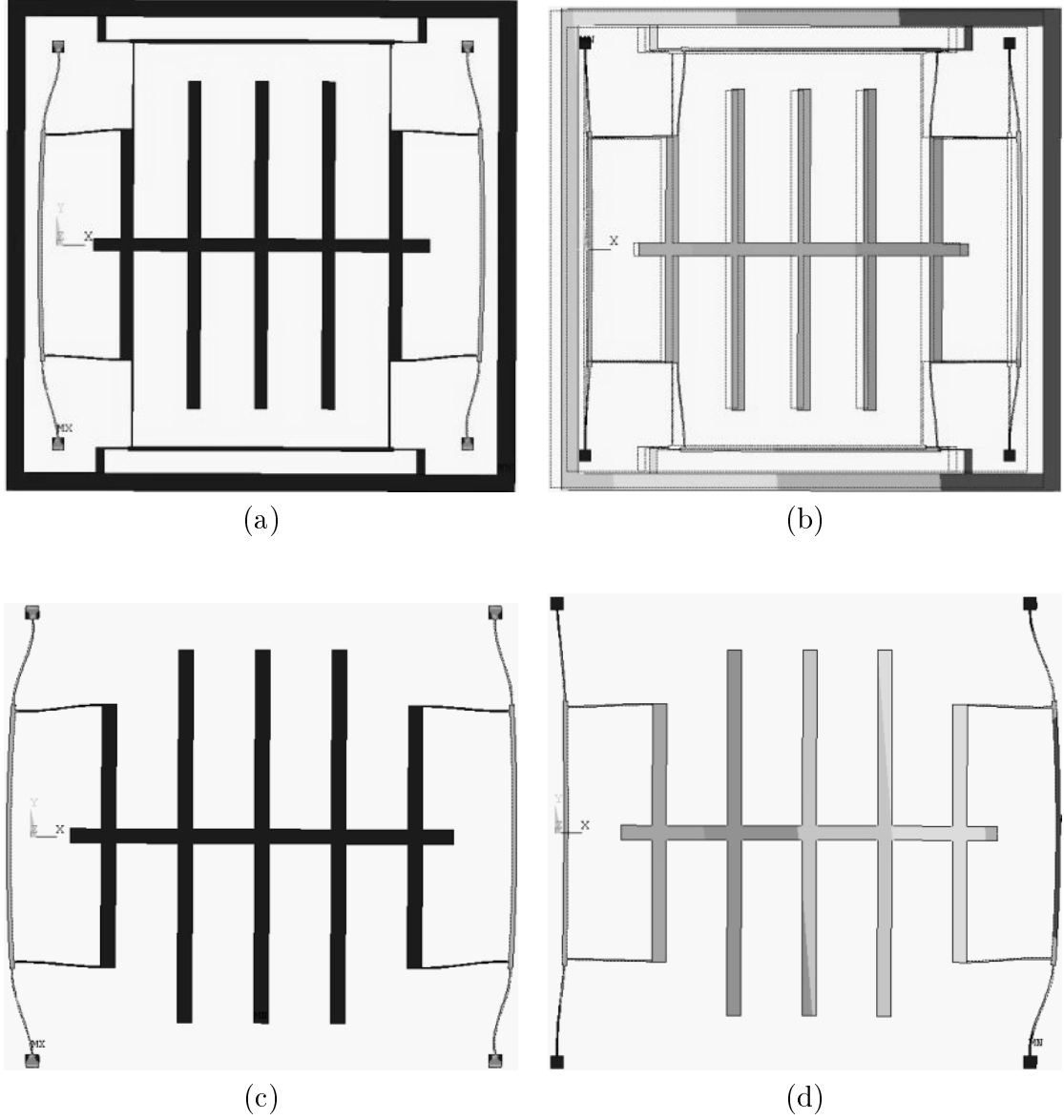


Figure 4.4: (a) Finite element simulation of the device with a uniform temperature loading of $100^\circ C$. Thermally induced localized stresses were observed only in the drive-direction beam elements of active mass, effecting only k_{1x} . (b) Static finite element analysis of the thermally loaded system with the modified Young's modulus. (c) Finite element analysis of a conventional gyroscope with similar geometry, under the same thermal loading. (d) Static analysis of the conventional design indicate the localized stresses leading to frequency mismatch between the drive and the sense resonant frequencies.

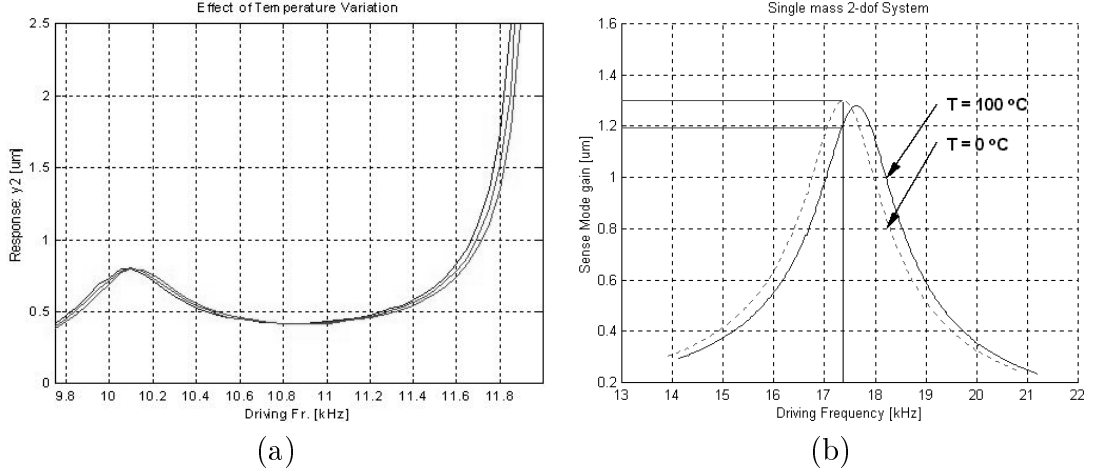


Figure 4.5: (a) Simulation of the proposed design's dynamical system with the perturbed parameters due to thermal loading was performed, indicating less than 0.9% gain deviation. (b) Simulation of the conventional design with the perturbed parameters indicates 7% gain error for the same thermal loading.

$$k_{2x} = \frac{Etw\kappa_y^2}{12L_{2x}} \left[1 - \frac{2w}{\beta_{2x}L_{2x}} \frac{\cosh(\frac{\kappa_y L_{2x}}{w}) - 1}{\sinh(\frac{\kappa_y L_{2x}}{w})} \right]^{-1} \quad (4.6)$$

$$k_{2y} = \frac{Etw\kappa_x^2}{12L_{2y}} \left[1 - \frac{2w}{\beta_{2y}L_{2y}} \frac{\cosh(\frac{\kappa_x L_{2y}}{w}) - 1}{\sinh(\frac{\kappa_x L_{2y}}{w})} \right]^{-1}. \quad (4.7)$$

where $\kappa_x = \sqrt{12\varepsilon_x}$, $\kappa_y = \sqrt{12\varepsilon_y}$ are the dimensionless strain factors for beam bending, and $\beta_{1x} = \frac{L_{1x}w}{\kappa_y}$, $\beta_{1y} = \frac{L_{1y}t}{\kappa_x}$, $\beta_{2x} = \frac{L_{2x}w}{\kappa_y}$, $\beta_{2y} = \frac{L_{2y}t}{\kappa_x}$.

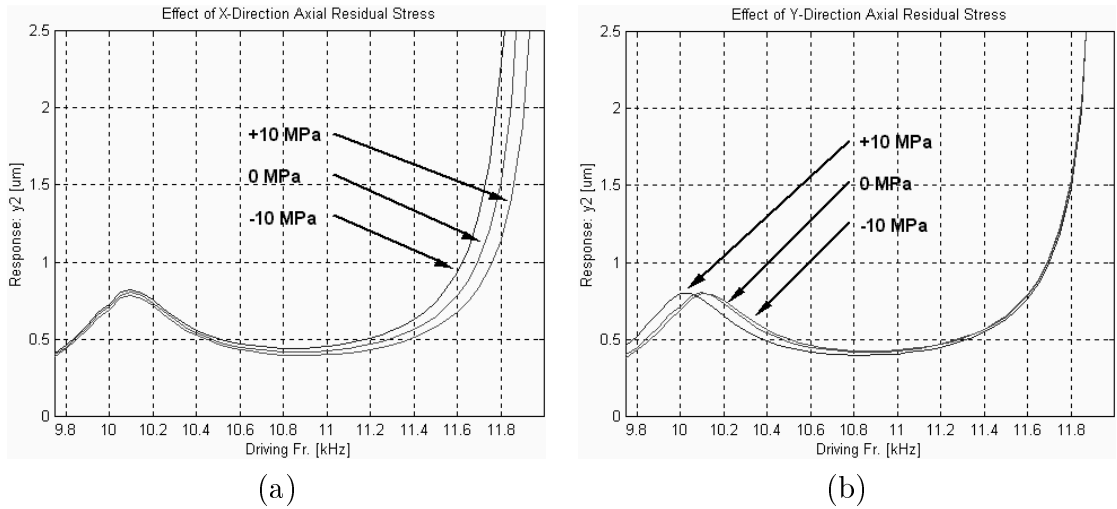


Figure 4.6: Effect of residual stresses (a) in x-direction, (b) in y-direction.

However, an axial residual stress ε_x in the x direction effects the sense-direction spring rates (k_{1y} and k_{2y}) of the same order, and an axial residual stress ε_y in the y direction effects the drive-direction spring rates (k_{1x} and k_{2x}) of the same order as well. In result, the overall system response is less sensitive to residual stresses (Fig. 4.6). To compare the sensitivity

of the proposed device to the conventional approach, the designed system and a single mass gyroscope with the same geometry of the isolated active mass-spring system were simulated with a 10 MPa compression residual stress. The single-mass system experienced approximately 2.5% gain reduction, while the proposed device experienced less than 0.2% deviation in the gain.

4.5 Conclusion

In this section, sensitivity analysis of the proposed design was studied. The effects of realistic parameter variations on the system response are investigated, and the robustness of the proposed system against these variations is compared to the conventional designs. Sensitivity analysis revealed that, for the same thermal loading, the device produces 87% less error than conventional gyroscopes. Moreover, the proposed design was shown to be approximately 12 times less sensitive to residual stresses, and 20 times less sensitive to fabrication variations than conventional gyroscopes.

Chapter 5

Conclusion and Future Work

With the advances in micromachining technologies, low cost inertial micro-sensors on-a-chip are beginning to enter the market. Derived from the conventional Integrated Circuit (IC) fabrication technologies, micromachining processes allow mass-production of microstructures with moving parts on a chip controlled by electronics integrated on the same chip. Optimistic projections predict that in a near future, expensive and bulky conventional inertial sensors will be replaced by their low-cost and micro-sized counterparts without any compromise in performance. Micromachined gyroscopes could potentially provide high accuracy rotation measurements leading to a wide range of applications including navigation and guidance systems, automotive safety systems, and consumer electronics. However, truly low-cost and high-performance devices are not on the market yet, and the current state of the art micromachined gyroscopes require an order of magnitude improvement in performance, stability, and robustness.

5.1 Contribution

In this thesis, a novel micromachined vibratory rate gyroscope design approach was developed to overcome the limitations of the existing micromachined gyroscope designs. The proposed design concept suggests the use of two coupled independently vibrating proof masses to form a 4-DOF dynamical system. Computer modeling of the proposed design indicates over 15 times increase in the bandwidth of the system as compared to the conventional gyroscopes. In addition, significantly reduced sensitivity of the gyroscope to structural and thermal parameter fluctuations and damping is demonstrated. By utilizing the disturbance-rejection capability of the inertial system, improved robustness is achieved without further sophistication in control electronics. All these advantages of the presented design might relax strict fabrication tolerances and packaging requirements, reducing production cost of micromachined gyroscopes without compromising performance.

5.2 Future Work

The design concept was demonstrated by computer modeling to provide improved robustness by investigating the effects of realistic parameter variations on the system response, and comparing the sensitivity of the proposed system to the conventional designs. However, these results have not been verified experimentally yet. Thus, the first step of future work will involve experimental evaluation of performance of the fabricated prototype gyroscopes. The next step will be to develop the control strategies which will provide the highest possible performance.

5.2.1 Experimental Evaluation of the Prototype Designs

To evaluate the performance of the fabricated prototype gyroscope designs, first balanced comb-drive strategy will be employed to drive the system into oscillations in the drive-mode. This driving scheme can be realized using the setup illustrated in Figure 5.1.

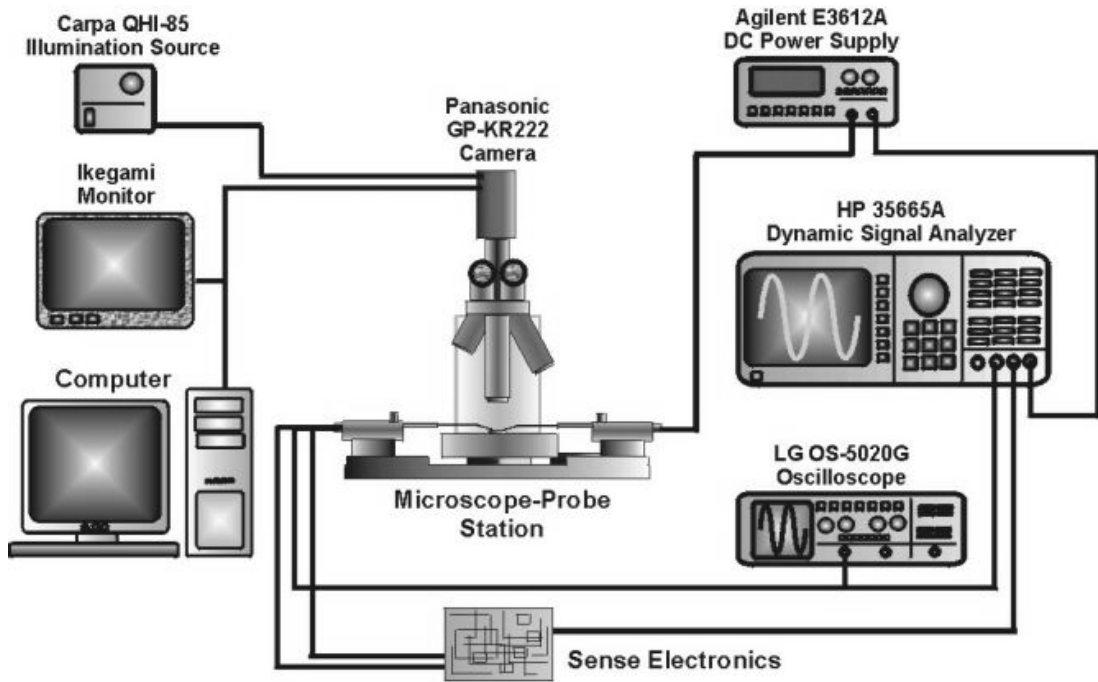


Figure 5.1: Experimental setup for experimental evaluation of prototype gyroscopes.

Then the response of the gyroscope to input angular rate has to be sensed. Since the deflection of the second mass due to the Coriolis force is converted into capacitance change by the sense capacitors, this capacitive signal should be converted into an output voltage signal with enough amplitude. The basic task of the sense electronics is to provide this conversion. Small changes in capacitance due to deflection result in a displacement current that flows through the sense capacitors. This current can be sensed employing an integrator in a sense amplifier configuration [2].

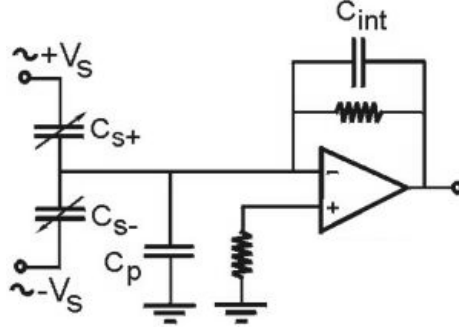


Figure 5.2: The implementation of the integrator for capacitive sensing.

5.2.2 Control Issues

Since the Coriolis response of the second mass in the sense direction is directly correlated to the drive oscillation amplitude, it is crucial that the second mass is driven into forced oscillation in drive direction with a known constant amplitude. Thus, the primary task of the control electronics will be to assure constant amplitude oscillation for the second mass with the required driving frequency.

Moreover, an ideal gyroscope should be sensitive to only the input angular rate. However, in practice, micromachined gyroscopes are sensitive not only to the measured angular rate, but also to fabrication imperfections and undesirable excitations. This defines another major task of the control system as compensation for these imperfections.

Control of Oscillations in Drive Mode

The Coriolis force which excites the second mass in the sense direction is described by

$$F_{Coriolis} = 2m_2\Omega\dot{x}_2. \quad (5.1)$$

Since the Coriolis force is proportional to the linear velocity of the second mass, it is also proportional to the oscillation amplitude. To assure an accurate angular rate measurement, the drive mode oscillation amplitude of the second mass should be kept constant by the drive electronics.

Employing balanced comb-drive strategy to drive the system is the simplest solution from the implementation aspect. However, since it is vital to have a known drive-direction oscillation amplitude of the second mass for accurate rate measurement, the error in the oscillation amplitude should be minimized. When the gyroscope is driven using an open-loop control, any change in system parameters will cause errors in the oscillation amplitude, leading to erroneous rate measurement. Thus, it is necessary to have feedback control to achieve the desired oscillation amplitude.

To provide the feedback signal for the control system, comb structures have to be built in the second mass (Figure 5.3), and a trans-resistance amplifier has to be incorporated into the control loop to convert the displacement current generated by the oscillating second mass to

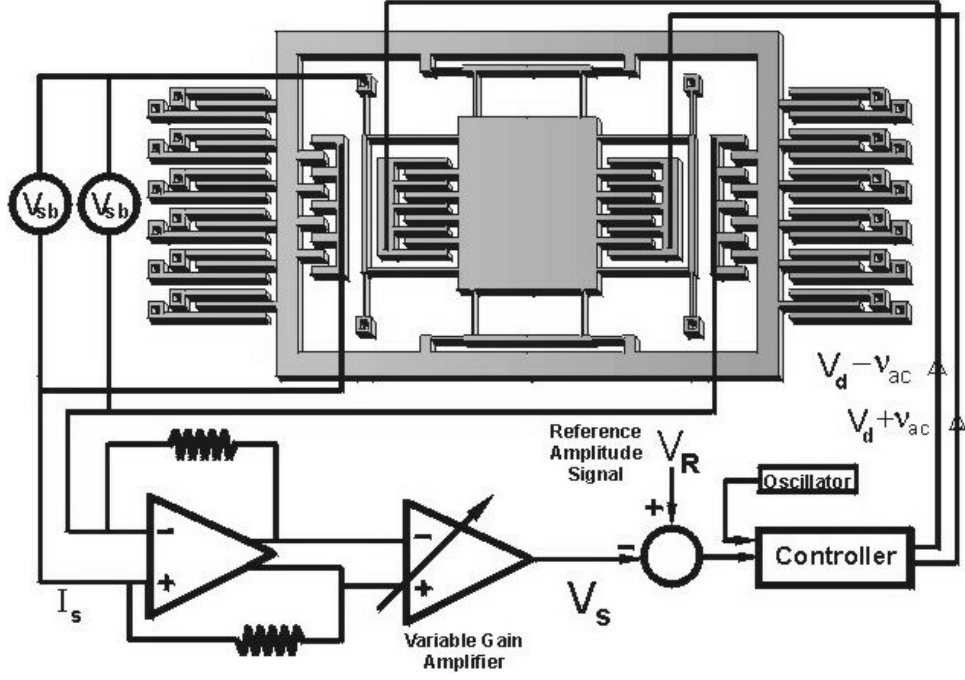


Figure 5.3: Closed-loop driving scheme of the dual-mass gyroscope.

an output feedback voltage. Then, the control law has to be defined to drive the error signal, which is the difference of the output voltage of the trans-resistance amplifier and a reference voltage determining the desired oscillation amplitude [18].

Compensation of Fabrication Imperfections

An ideal gyroscope should be sensitive only to the input angular rate. However, in practice, micromachined vibratory gyroscopes are sensitive not only to the measured angular rate, but also to fabrication imperfections. Due to lack of perfect alignment of the intended and the actual principle axes of oscillation, anisoelectricity in the gyroscope structure occurs, causing dynamic cross-coupling between the drive and sense directions.

The resulting dynamic cross-coupling stiffness and damping terms are the major factors that limit the performance of the gyroscope. Thus, the control system should eliminate the effects of the fabrication imperfections, and render the gyroscope sensitive only to the input angular rate. Consequently, the next step in the control system design will be the development of a controller that will compensate for the cross-coupling between the drive and sense directions.

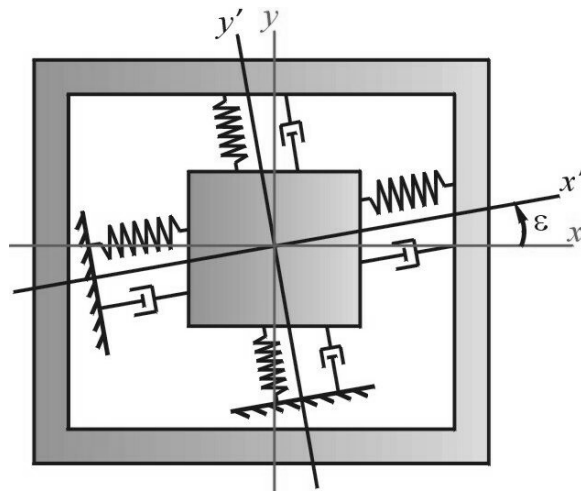


Figure 5.4: Modeling of anisotropy, the mis-alignment of the intended and the actual principle axes of oscillation.

Bibliography

- [1] N. Yazdi, F. Ayazi, and K. Najafi. Micromachined Inertial Sensors. *Proc. of IEEE*, Vol. 86, No. 8, August 1998.
- [2] W.A. Clark. Micromachined Vibratory Rate Gyroscope. *Ph.D. Thesis, BSAC, U.C. Berkeley*, 1994.
- [3] W.A. Clark, R.T. Howe, and R. Horowitz. Surface Micromachined Z-Axis Vibratory Rate Gyroscope. *Proceedings of Solid-State Sensor and Actuator Workshop*, June 1994.
- [4] E. Netzer, and I. Porat. A Novel Vibratory Device for Angular Rate Measurement. *Journal of Dynamic Systems, Measurement and Control*, Dec. 1995.
- [5] A. Shkel, R.T. Howe, and R. Horowitz. Micromachined Gyroscopes: Challenges, Design Solutions, and Opportunities. *Int. Workshop on Micro-Robots, Micro-Machines and Systems, Moscow, Russia*, 1999.
- [6] A. Shkel, R. Horowitz, A. Seshia, S. Park and R.T. Howe. Dynamics and Control of Micromachined Gyroscopes *American Control Conference, CA*, 1999.
- [7] US 5,992,233. Clark. Micromachined z-Axis Vibratory Gyroscope. Nov. 1999.
- [8] US 6,122,961. Geen, and Carow. Micromachined Gyros. Sept. 2000.
- [9] C.W. Dyck, J. Allen, R. Hueber. Parallel Plate Electrostatic Dual Mass Oscillator. *Proceedings of SPIE SOE, CA*, 1999.
- [10] L. Lin, R.T. Howe, and A.P. Pisano. Microelectromechanical Filters for Signal Processing. *Journal of Microelectromechanical Systems*, Vol. 7, Sept. 1998.
- [11] C. Acar and A. Shkel. Wide Bandwidth Micromachined Gyroscope to Measure Rotation. *Patent pending, UCI Office of Technology Alliances*, Case No:2001-140-1.
- [12] W.C. Young. Roark's Formulas for Stress & Strain. *McGraw-Hill, Inc.*, 93-156, 1989.
- [13] B.E. Boser. Electronics For Micromachined Inertial Sensors. *Proc. Transducers*, 1997.

- [14] Lemkin. Micro Accelerometer Design with Digital Feedback Control. *Ph.D. Thesis, BSAC, U.C. Berkeley*, 1997.
- [15] A. Seshia. Design and Modeling of a Dual Mass SOI-MEMS Gyroscope. *M.S. Thesis, BSAC, U.C. Berkeley*, 1999.
- [16] C. Acar, A. Shkel. A Design Approach for Robustness Improvement of Rate Gyroscopes. *Modeling and Simulation of Microsystems Conference*, March 2001.
- [17] C. Acar, A. Shkel. Microgyroscopes with Dynamic Disturbance Rejection. *SPIE Conference on Smart Electronics and MEMS*, March 2001.
- [18] C. Acar, S. Eler, and A. Shkel. Concept, Implementation, and Control of Wide Bandwidth MEMS Gyroscopes. *American Control Conference*, June 2001.
- [19] D.A. Koester, R. Mahadevan, B. Hardy, and K.W. Markus. MUMPs Design Handbook, Revision 5.0. *Cronos Integrated Microsystems*, 2000.

Appendix A

Gyroscope Simulation MATLAB Codes

A.1 gyroparameters.m

```
%Gyro Suite Module 1
%Gyroscope Parameter Initialization
%gyroparameters.m
%-----
clear all;clc;

wz = 1 * (2 * pi / 360) %measured angular rate = 1 deg/sec
p = 150 e-3 %Operation Pressure [ torr ]
mu_vis = 3.7 e-4 * p; %Air Viscosity
dens = 2.33 e3; %Density of Polysilicon
E = 170 e9; %PolySi Young's Modulus [ Pa]
th = 2 e-6; %Structure thickness
z0 = 2 e-6; %Elevation of structure

% Mass 1 parameters:
Amass1 = 37968 e-12 * 2; %Area of Mass1 [ m2]
m1 = Amass1 * th * dens; %Mass of Mass1 [ kg]

% Mass 2 parameters:
Amass2 = 95962 e-12 * 2; %Area of Mass2 [ m2]
m2 = Amass2 * th * dens; %Mass of Mass2 [ kg]

% Spring Structures:
wspring = 2 e-6; %spring width
L1x = 130 e-6; %spring length, M1, drive [m]
L1y = 130 e-6; %spring length, M1, sense [m]
L2x = 137 e-6; %spring length, M2, drive [m]
L2y = 38 e-6; %spring length, M2, sense [m]

k1x = 4 * E * th * wspring ^ 3 / L1x ^ 3 %spring const. M1, drive [ N/m]
k1y = 4 * E * th * wspring ^ 3 / L1y ^ 3 %spring const. M1, sense [ N/m]
k2x = 4 * E * th * wspring ^ 3 / L2x ^ 3 %spring const. M2, drive [ N/m]
k2y = 4 * E * th * wspring ^ 3 / L2y ^ 3 %spring const. M2, sense [ N/m]

% Ratios:
beta = m2 / m1; %Mass ratio
sigy = k2y / k1y; %y spring const. ratio
sigx = k2x / k1x; %x spring const. ratio

%Comb Drive Properties:
ncomb = 31 * 2 * 6 + 21 * 4 + 18 * 4; %total 528 fingers
ncomb_one = ncomb / 2; %264 fingers in one direction

wcomb = 2 e-6; %comb finger width
ycomb = 2 e-6; %distance between combs
lcomb = 20 e-6; %comb finger total length
Acomb = wcomb * lcomb; %footstep area per finger
Acomb_tot = ncomb * wcomb * lcomb; %total footstep area of combs
m_comb = Acomb_tot * th * dens; %total mass of combs

lcomb_ov = 15 e-6; %comb finger overlap length
Acomb_ov = th * lcomb * 2; %overlap area per finger (2 sides)
Acomb_tot_ov = Acomb_ov * ncomb; %total overlap area of combs (2 sides)
r_m1_mcomb = m_comb / m1; %mass ratio of Combs/m1

%Air-Gap Capacitor Properties:
ncap = 12 * 4 + 20 * 2 * 2; %total 176 caps for gyro2
wcap = 3 e-6; %capacitor width
ycap = 3 e-6; %distance between combs
lcap = 130 e-6; %capacitor total length
Acap = wcap * lcap; %footstep area per finger
Acap_tot = wcap * lcap; %total footstep area of capacitors
m_cap = Acap_tot * th * dens; %total mass of capacitors
r_m2_mcap = m_cap / m2; %mass ratio of Capacitors/m2

lcap_ov = 120 e-6; %capacitor overlap length
Acap_ov = th * lcap * 2; %overlap area per finger (2 sides)
Acap_tot_ov = Acap * ncap; %total overlap area of caps (2 sides)
```

A.2 resonant freq.m

```
%Gyro Suite Module 2
%Gyroscope Resonant Frequency Calculator
%resonant_freq.m
%-----
wlx = sqrt(k1x / m1); %res. freq. M1, drive [ rad/sec]
wly = sqrt(k1y / m1); %res. freq. M1, sense [ rad/sec]
```

```

w2x = sqrt(k2x/m2);
w2y = sqrt(k2y/m2);
%res: freq: M2; drive [rad/sec]
%res: freq: M2; sense [rad/sec]

f1x = w1x/(2*pi)/1000;
f1y = w1y/(2*pi)/1000;
%res: freq: M1; drive [kHz]
%res: freq: M1; sense [kHz]
f2x = w2x/(2*pi)/1000;
f2y = w2y/(2*pi)/1000;
%res: freq: M2; drive [kHz]
%res: freq: M2; sense [kHz]

% Dual Mass System Peak Locations: -----
gamx=f2x/f1x;
gamy=f2y/f1y;

cfhx = sqrt((1/gamx^2 + (1+beta) + sqrt((1/gamx^2 + (1+beta))^2 - 4/gamx^2))/2);
cfly = sqrt((1/gamy^2 + (1+beta) + sqrt((1/gamy^2 + (1+beta))^2 - 4/gamy^2))/2);

f_oh_x = f2x * cfhx;
f_oh_y = f2y * cfhy;

```

A.3 gyro damping.m

```

%Gyro Suite, Module 3
%Damping Estimations of the Dual Mass Gyro
%gyrodamping.m
%-----

% Mass 1
%couette flow between M1 and substrate:
bm1_subst = mu_vis * Amass1/z0;

%couette flow between comb drive fingers:
bm1_comb = mu_vis * Acomb_tot_ov / ycomb;

% Total damping for M1 in Drive dir:
bm1 = bm1_subst + bm1_comb;
c1x = bm1;

% Mass 2
%couette flow between M2 and substrate:
bm2_subst = mu_vis * Amass2/z0;

%couette flow between capacitor fingers:
bm2_cap_couette = mu_vis * Acap_tot_ov / ycap;

% Squeeze film damping between capacitor fingers:
Acap_tot_ov_sq = Acap_tot_ov^2;
bm2_cap_squeeze = (7 * mu_vis * Acap_tot_ov_sq * th^2) / ycap^2;

% Total damping for M2 in Drive dir:
bm2_drive = bm2_subst + bm2_cap_couette;
c2x = bm2_drive;

% Total damping for M2 in Sense dir:
bm2_sense = bm2_subst + bm2_cap_squeeze;
c2y = bm2_sense;

%Damping ratio in drive direction:
mu = c2x/c1x;

% Q factors:
Q1x = w1x*m1/bm1;
Q2x = w2x*m2/bm2_drive;
Q2y = w2y*m2/bm2_sense;

Q1xnew_p = w1x * dens / 3.7e-4 / (1/z0 + 2*r_m1_mcomb/wcomb);
Q1xnew = Q1xnew_p * p;
%clx=w1x*m1/Q1xnew

```

A.4 electronic interface.m

```

%Gyro Suite, Module 4
%Dual Mass Gyroscope Electronic Interface Model
%electronic_interface.m
%-----

eo=8.854e-12;
Vdc=5;
vac=5;
%DC Bias Voltage Magnitude
%AC Alternating Voltage Magnitude

%Differential Comb Drive Scheme:
F0 = 4*eo*th / ycomb * Vdc * vac * ncomb_one;

%One Direction Comb Drive Scheme:
%F = 1/2*eo*t/d * Vdc^2 * N

```

A.5 single gyro two dof.m

```

% Gyro Suite, Module 5
% Single-Mass 2-DOF Gyroscope State-Space form:
% X: drive Y: Sense
% single_gyro_two_dof.m
%-----
c1x=c1x*1.5;
%k1x=k1x*1.1;

m = m1; kx = k1x; ky = k1y;
cx = c1x; cy = c1y;

wn = sqrt(ky/m); %sense dir nat. freq.
fn = wn/2000/pi; % kHz
zeta = cx/(2*m*wn);
fd = fn; % Forcing Freq: F= Fo sin(omega t) ; kHz
omega = fd*2000*pi;

%differential combs:
eo=8.854e-12;
th=2e-6;
d=2e-6;
Vdc=10;

```

```

v=5;
N=270;
Fo= 4* eo * th/d * Vdc * v * N;
wx = sqrt(kx/m);
wy = sqrt(ky/m);
lam=wx/wy;
Qx=m*wx/cx;
Qy=m*wy/cy;
xm=Fo*Qx/kx*1e6 %magnitude of x at resonance [um]
ym= 2*n*wz*wx*xm/ky/sqrt((1-lam^2)^2+lam^2) % output at resonance
yma= 2*Fo*m/wx/cx/cy*wz*1e6
ymaa= wz*xm/wx/zeta
% State-Space :
a = [0 0 1 0; 0 0 0 1;
      -kx/m 0 -cx/m 0;
      0 -ky/m -2*wz -cy/m];
b = [0 0 Fo/m 0]';
c = [0 1 0 0]; % output : y
d = [1 0 0 0]; % output : x
sys = ss(a,b,c,d);
t=0:0.000005:0.002;
u=sin(omega*t);
figure(1); clf;
lsim(sys,u,t);
i=0;
for alfa=0.8:0.001:1.2
    i=i+1;
    fdrive(i)=fd*alfa; % Forcing Freq: F= Fo sin(omega t) ; kHz
    omega = fdrive(i)*2000*pi;
    u=sin(omega*t);
    [Y,T]=lsim(sys,u,t);
    sy=size(Y); syup=ceil(sy*6/10); sylo=ceil(sy*9/10);
    gainm(i)=max(abs(Y(syup:sylo)))*1e6; % output in um
end
figure(2);
%clf;
hold on;
plot(fdrive,gainm);
title('Single mass 2-dof System');
xlabel('Driving Frequency [kHz]');
ylabel('Sense Mode gain [um]');

```

A.6 dual drive oscillator.m

```

%Gyro Suite Module 6
%Dual Mass Gyroscope Drive Direction Oscillator Model
%dual_drive_oscillator.m
-----
Adrive=[0 0 1 0; 0 0 0 1;
         -(k1x+k2x)/m1-k2x/m1 -c1x/m1 0;
         k2x/m2 -k2x/m2 0 -c2x/m2];
Bdrive=[0 0 Fo/m1 0]';
Cdrive_m2=[0 0 0 0];
Cdrive_m1=[1 0 0 0];
Ddrive=0;
SYSdrive_m2 = ss(Adrive,Bdrive,Cdrive_m2,Ddrive);
SYSdrive_m1 = ss(Adrive,Bdrive,Cdrive_m1,Ddrive);
%State-Space of Single M2 system:
Asingle=[0 1;
          -k2x/m2 -c2x/m2];
Bsingle=[0 Fo/m2]';
Csingle=[1 0];
Dsingle=0;
SYSsingle = ss(Asingle,Bsingle,Csingle,Dsingle);
om=1*2000*pi:1*200*pi:35*2000*pi % Frequency array [kHz]
frq=om/2000/pi;
x1=freqresp(SYSdrive_m1,om);
x1abs=abs(x1);
x1ang=angle(x1);
x2=freqresp(SYSdrive_m2,om);
x2abs=abs(x2);
x2ang=angle(x2);
xsingle=freqresp(SYSsingle,om);
xsingleabs=abs(xsingle);
xsingleang=angle(xsingle);
sizex=size(x1);
for i=1:sizex(3)
    x1absi(i)=x1abs(:,i)*1e6;
    x2absi(i)=x2abs(:,i)*1e6;
    xsingleabsi(i)=xsingleabs(:,i)*1e6;
    x1angi(i)=x2ang(:,i);
    x2angi(i)=x1ang(:,i);
end
rat(i)=x2absi(i)/x1absi(i);
figure(1); clf; hold on;
plot(frq,x2absi);
plot(frq,x1absi);
plot(frq,xsingleabsi);
%plot(frq,xsingleabsi);
title('Dual Mass Oscillator, x1 and, x2 Magnitude');
xlabel('Driving Fr. [kHz]'); ylabel('Magnitude [um]');
figure(2); clf; hold on;
plot(frq,x2angi);
plot(frq,x1angi);
title('Dual Mass Oscillator, x1 and, x2 Phase');
xlabel('Driving Fr. [kHz]'); ylabel('Phase');
figure(3); clf;
semilogx(frq,rat);
title('Dual Mass Oscillator, x1 and, x2 Magnitude Ratio');
xlabel('Driving Fr. [kHz]'); ylabel('Magnitude Ratio');

```

```

figure(4);clf;
fd=0.00001:0.05; % ave. Forcing Frequency ; kHz
alfa=1;
fdrive=fd*alfa; % Forcing Frequency ; kHz
omega=fdrive*2000*pi;
u=sin(omega*t);
ssim('Single Mass Oscillator');

```

A.7 dual drive osc volt.m

```

%Gyro Suite Module 7
%Dual Mass Gyroscope Drive Direction Oscillator Model
%Voltage-Amplitude analysis
%dual_drive_osc_volt.m
%-----

% Vdc increased , vac = 5V
i=0;
for Vdc=5:2:100; %DC Bias Voltage Magnitude
    i=i+1;
    V1(i)=Vdc;
    F0=4*eo*th/ycomb*Vdc*vac*ncomb_one;
    Adrive=[0 0 1 0;0 0 0 1;
            -(k1x+k2x)/m1 k2x/m1 -c1x/m1 0;
            k2x/m2 -k2x/m2 0 -c2x/m2];
    Bdrive=[0 0 F0/m1 0]';
    Cdrive_m2=[0 0 0 0];
    Cdrive_m1=[1 0 0 0];
    Ddrive=[0];
    SYSdrive_m1=ss(Adrive,Bdrive,Cdrive_m1,Ddrive);

    x1v=freqresp(SYSdrive_m1,w2x);
    x1absv=abs(x1v);
    x2v=freqresp(SYSdrive_m2,w2x);
    x2absv=abs(x2v);
    x1absv(i)=x1absv(:,:1)*1e6;
    x2absv(i)=x2absv(:,:1)*1e6;
end

figure(1);clf;hold on;
plot(V1,x1absv);
plot(V1,x2absv);
title('Dual Mass Oscillator ; x1 and x2 Magnitude');
xlabel('Bias Voltage [V]'); ylabel('Magnitude [um]');

% Vdc and vac are increased , Vdc = vac
i=0;
for Vdc=5:0.5:25; %DC Bias Voltage Magnitude
    i=i+1;
    V1(i)=Vdc;
    F0=4*eo*th/ycomb*Vdc^2*ncomb_one;
    Adrive=[0 0 1 0;0 0 0 1;
            -(k1x+k2x)/m1 k2x/m1 -c1x/m1 0;
            k2x/m2 -k2x/m2 0 -c2x/m2];
    Bdrive=[0 0 F0/m1 0]';
    Cdrive_m2=[0 0 0 0];
    Cdrive_m1=[1 0 0 0];
    Ddrive=[0];
    SYSdrive_m1=ss(Adrive,Bdrive,Cdrive_m1,Ddrive);

    x1v2=freqresp(SYSdrive_m1,w2x);
    x1absv2=abs(x1v2);
    x2v2=freqresp(SYSdrive_m2,w2x);
    x2absv2=abs(x2v2);
    x1absv2(i)=x1absv2(:,:1)*1e6;
    x2absv2(i)=x2absv2(:,:1)*1e6;
end

figure(2);clf;hold on;
plot(V1,x1absv2);
plot(V1,x2absv2);
title('Dual Mass Oscillator ; x1 and x2 Magnitude');
xlabel('Bias and AC Voltage ; Vdc = vac [V]'); ylabel('Magnitude [um]');

```

A.8 full three dof ss.m

```

% Gyro Suite Module 8
% 3 DOF System State-Space form, x1 = xo cos(omega t)
% X : drive, Y : Sense (changed, s sig1 with sig2)
% full_three_dof_ss.m
%-----
c1x=c1x/2;
fdrive=10; % Forcing Frequency : x1 = xo cos(omega t) ; kHz
omega=fdrive*2000*pi;
xo=1e-6; %Mass 1 drive amplitude
c1x=1e-7;
c2=1e-7;
sig1=sigx; % spring const. ratio
sig2=sigy; % spring const. ratio
wn=wlv; %sense dir nat. freq.
zeta=c1x/(2*m1*wn);
s=k2x/k2y;
%zeta=1
% State-Space:
% State: x=[x2 y1 y2 x2. y1. y2.]
a=[0 0 0 1 0 0;
    0 0 0 0 1 0;
    0 0 0 0 0 1;

```



```

    (wz^2-sig2*wn^2/beta)/0 0 0 0 (-2*wz);
    0 (wz^2-(1+sig1)*wn^2)/(sig1*wn^2) 0 (-2*zeta*wn*(1+mu)) (2*zeta*wn*mu);
    0 (sig1*wn^2/beta) (wz^2-sig1*wn^2/beta) (2*wz) (2*zeta*wn*mu/beta)
    (-2*zeta*wn*mu/beta)];
b = [0 0 0 (sig2*wn^2/beta) 0 0 ; 0 0 0 0 (2*wz) 0]';
c = [0 0]; % output : y2
d = [0 0];
sys = ss(a,b,c,d);
t = 0:0.00002:0.04;
%u = [(x0*cos(omega*t)) ; (-x0*omega*sin(omega*t))];
figure(3); clf;
%lsim(sys,u,t);
%title('Response y2 at 10 kHz');
i=0;
for alfa = 0.98:0.005:1.2
    i=i+1;
    fdrive(i) = 10*alfa; % Forcing Frequency : x1 = x0 cos(omega t) ; kHz
    omega = fdrive(i)*2000*pi;
    u = [x0*cos(omega*t) ; (-x0*omega*sin(omega*t))];
    [Y,T] = lsim(sys,u,t);
    %lsim(sys,u,t);
    %zoom;
    sy = size(Y);
    syup = ceil(sy*6/10);
    sylo = ceil(sy*9/10);
    gainm(i) = max(abs(Y(syup:sylo))); %gain [m]
    pgain(i) = gainm(i)*omega*zeta/wz/x0;
end
figure(1);
%clf;
%hold on;
%plot(fdrive,pgain)
%axis([0 18.0 1e-5]);
%title('Deflection y2 vs. Driving Freq. y2/W');
%xlabel('Driving Fr. [ kHz]'); ylabel('y2 / W');
figure(2);
%clf;
%hold on;
%plot(fdrive,gainm*1e10)
%axis([0 18.0 1e-2]);
%title('Deflection y2 vs. Driving Freq. y2');
%xlabel('Driving Fr. [ kHz]'); ylabel('y2 [um]');

```

A.9 full three dof var.m

```

% Gyro Suite . Module 9
% 3 DOF System Analytic Solution s x1 = x0 cos(omega t)
% X : drive Y : Sense (changed s sig1 with sig2)
% full_three_dof_var.m
%-----
% Fig 4 of paper "A Novel Vibratory Device for Ang. Rate Meas."
% by Netzer, Porat
% The effect of change in any parameter can be observed by selecting
% the iteration variable and the upper-lower bounds....
y0 = 1e-6/10;
wn = wly;
omz = wz;
fdrive = 10; % Forcing Frequency : x1 = x0 cos(omega t) ; kHz
omega = fdrive*2000*pi;
zeta = cix/(2*m1*wn);

alfa = omz/wn;
rfrq = omega/wn; % spring const : ratio
sig1 = sigx; % spring const : ratio
sig2 = sigx;

%Nominal example values:
wn = 7000*2*pi;
beta = 3;
sig1 = 40;
sig2 = 1;
zeta = 0.1;
alfa = omz/wn;

%Choose the parameter to iterate to see the effect of its change:
%Set the upper and lower bounds
varmid = zeta;
varmin = 0.05;
varmax = 0.15;
varmin = 0.5*varmid;
varmax = 1.5*varmid;
varinc = (varmax-varmin)/4;

m=0;
for zeta = varmin:varinc:varmax %Select the parameter
    m=m+1;
    var(m)=zeta; % for monitoring the values of the parameter
    i=0;
    for rfrq = 0.4 : 0.001 : 0.7
        i=i+1;
        B11 = -rfrq^2 - (2*alfa^2 + 1 + sig1 + (2*rfrq*zeta*(1+mu))*j);
        B12 = -sig1 - (2*rfrq*zeta*mu)*j;
        B21 = B12;
        B33 = 0;
        B32 = B13;
        B31 = beta * (-rfrq^2 - alfa^2) + sig1 + (2*rfrq*zeta*mu)*j;
        B22 = (2*beta*rfrq*alfa)*j;
        B32 = B23;
        B33 = beta * (-rfrq^2 - alfa^2) + sig2;
    B = [B11 B12 B13; B21 B22 B23; B31 B32 B33];
    W = omz * y0 / (omega*zeta);
    X = inv(B(1:2,1:2)) * [ alfa*rfrq*zeta*j ; beta*sig2*rfrq*zeta/B33*j ] * W;
    x2 = 2*abs(X(2));
    x1 = 2*abs(X(1));
    psi1 = angle(X(1)); % in radians
    psi2 = angle(X(2)); % in radians

```

```

X2Wi(i,m) = X2/W;
rfrqi(i) = rfrq;
end
end

figure(1);
plot(rfrqi,X2Wi(:,1), rfrqi,X2Wi(:,2), rfrqi,X2Wi(:,3), rfrqi,X2Wi(:,4),
rfrqi,X2Wi(:,5));
%axis([0.4 0.7 0 40]);
title('Response Gain vs Normalized Forcing Freq')
xlabel('Forcing Freq:  $X2^{wn}$ ')
ylabel('Resp. Gain:  $X2/W$ ')
grid;

var
figure(1);

```

Appendix B

ANSYS Parametric Design Language (APDL) Codes

B.1 dualgyrofea.inp

Finite Element Model of Dual-Mass Gyroscope, with thermal and modal analysis.

```
FINISH
/CLEAR
/GRAPH,POWER
/POST,ON
/PREP7

LX=136
LY=120

LX2=136
LY2=38

W=2
CONW=6
CONL=190

A=(106-20)/2
B=20
C=106
MLS=172
MLL=248
MASSL=106*5
MZW = 27

! MASS:
BLC4,CONW+LY-A,-10,MASSL,10
BLC4,CONW+LY-C+10-MLS,20,MLS
BLC4,CONW+LY-C+10-MLS,20,MLS
BLC4,CONW+LY+C-C,-10-MLL,20,MLL
BLC4,CONW+LY+C-C,-10-MLL,20,MLL
BLC4,CONW+LY+C+C-C,-10-MLL,20,MLL
BLC4,CONW+LY+C+C+C,-10-MLS,20,MLS

ARSYM,Y,ALL,,0,0
AADD,ALL
ASEL,U,,,ALL

! NEGATIVE PART:
! CONNECT
BLC4,0,-CONL,CONW,CONL
! X SPRING
BLC4,2,-CONL-LX,W,LX
! ANCHOR
BLC4,-6,-CONL-LX-18,18,18
! Y SPRING
BLC4,CONW,-CONL+4*W,LY,W
ARSYM,Y,ALL,,0,0
AADD,ALL
ASEL,U,,,ALL

! POSITIVE PART:
! CONNECT
BLC4,W+CONW-2+MASSL+LY+LY-A-A,-CONL,CONW,CONL
! X SPRING
BLC4,2+W+CONW-2+MASSL+LY+LY-A-A,-CONL-LX,W,LX
! ANCHOR
BLC4,-6+W+CONW-2+MASSL+LY+LY-A-A,-CONL-LX-18,18,18
! Y SPRING
BLC4,CONW+W+MASSL+LY-A-A-2,-CONL+4*W,LY,W
ARSYM,Y,ALL,,0,0
AADD,ALL
ASEL,U,,,ALL

BLC4,CONW+LY+B-2,-10-MLS-LX2,2,LX2
BLC4,CONW+LY+C+C+C,-10-MLS-LX2,2,LX2
```

```

BLC4, CONW+LY+B-7, -10-MLS-LX2-CONW, C+C+C+C-B+14, CONW
BLC4, CONW+LY+B-7-LY2, -10-MLS-LX2-CONW+2, LY2, 2
BLC4, CONW+LY+7+C+C+C+C, -10-MLS-LX2-CONW+2, LY2, 2
BLC4, CONW+LY+B-7-LY2-12, -10-MLS-LX2-CONW-36, 12, 40
BLC4, CONW+LY+7+C+C+C+C+LY2, -10-MLS-LX2-CONW-36, 12, 40
AADD, ALL
ARSYM, Y, ALL, , , , 0, 0
ASEL, U, , , ALL
! MASS 2
BLC4, -6-M2W-20, -360-M2W, 702+6+2*M2W+2*20, M2W
BLC4, -6-M2W-20, -360, M2W, 360
BLC4, 702+20, -360, M2W, 360
ARSYM, Y, ALL, , , , 0, 0
AADD, ALL
ASEL, S, , , ALL
AESIZE, 1, 3, , 1 ! mass1
AESIZE, 1, 1, , 1 ! mass2
AESIZE, 9, 5, , 1 ! spring 1
AESIZE, 10, 5, , 1 ! spring 1
AESIZE, 8, 5, , 1 ! spring 2
AESIZE, 1, 5, , 1 ! spring 2
ASEL, S, , , ALL
! ET, 1, SHELL63
! KEYOPT, 1, 1, 0
! KEYOPT, 1, 3, 0
! KEYOPT, 1, 3, 0
! RMORE, ,
et, 1, 42, , 3 ! Switch to structural element, PLANE42
r, et, 1, 63, , 3 ! Switch to structural element, PLANE42
real, 1 ! Plane stress with thickness of poly_t
mp, ex, 1, 169 e3 ! Modulus of elasticity
mp, nuxy, 1, 0.22 ! Poisson's ratio
mp, alpx, 1, 29 e-7 ! Coefficient of thermal expansion
UIMP, 1, EX, , , 1.5 e5,
UIMP, 1, NUXY, , , 2
UIMP, 1, DENS, , , 2333 E-18,
/SOLU
DL, 26, , ALL, 0
DL, 94, , ALL, 0
DL, 101, , ALL, 0
! FLX THE ANCHOR NODES
! NSEL, S, , , 138
! NSEL, A, , , 142
! NSEL, A, , , 673
D, ALL
ALLSEL, ALL, , , , ALL
/PREP7
! Mass 1 and springs
AMESH, 9
AMESH, 10
AMESH, 8
AMESH, 1
ESTIZE, 0.1,
AMESH, 13
AMESH, 11
! Mass1 - Substrate Spring connection (mass1)
NSEL, S, , , 470
NSEL, A, , , 494
ESEL, A, , , 472
CEINTF, , , ALL
NSEL, S, , , 591
NSEL, A, , , 613
ESEL, A, , , 473
CEINTF, , , ALL
NSEL, S, , , 328
NSEL, A, , , 304
ESEL, A, , , 476
CEINTF, , , ALL
NSEL, S, , , 207
NSEL, A, , , 183
ESEL, A, , , 475
CEINTF, , , ALL
ALLSEL, ALL
! Mass1 - Mass2 Spring connection (mass1)
NSEL, S, , , 138
NSEL, A, , , 135
ESEL, A, , , 472
CEINTF, , , ALL
NSEL, S, , , 105
NSEL, A, , , 103
ESEL, A, , , 473
CEINTF, , , ALL
NSEL, S, , , 158
NSEL, A, , , 134
ESEL, A, , , 476
CEINTF, , , ALL
NSEL, S, , , 860
NSEL, A, , , 829
ESEL, A, , , 475
CEINTF, , , ALL
ALLSEL, ALL
! Mass2 - Mass1 Spring connection (mass2)

```

```

! Top element
NSEL,S,,,1435
NSEL,A,,,1436
NSEL,A,,,1437
NSEL,A,,,1427
NSEL,A,,,989
CENTF,,ALL

NSEL,S,,,1556
NSEL,A,,,1557
NSEL,A,,,1558
NSEL,A,,,1548
NSEL,A,,,989
CENTF,,ALL

! Bottom element
NSEL,S,,,1031
NSEL,A,,,1032
NSEL,A,,,1033
NSEL,A,,,991
CENTF,,ALL

NSEL,S,,,902
NSEL,A,,,911
NSEL,A,,,912
NSEL,A,,,910
NSEL,A,,,991
CENTF,,ALL

ALLSEL,ALL

/SOLU
*
ANTYPE,2
!
*
MODOPT,SUBSP,6
EQSLV,FRONT
EXPAND,0,,0
LUMPM,0
PSTRES,0
!
*
MODOPT,SUBSP,6,100,100000,,OFF
RIGID
SUBOPT,8,4,10,0,0,ALL
STATUS,SOLU
SOLVE

/EOF

```

B.2 singlegyrofea.inp

Finite Element Model of a Conventional Gyroscope, with thermal and modal analysis.

```

FINISH
/CLEAR
/GBA,POWER
/POST,ON
/REP7

LX=136
LY=120
W=2
CONW=6
CONL=190

A=(106-20)/2
B=20
C=106
MLS=172
MLL=248
MASSL=106*5

! MASS:
BLC4,CONW+LY-A,-10,MASSL,10
BLC4,CONW+LY-C,10-MLS,20,MLS
BLC4,CONW+LY+C,-10-MLL,20,MLL
BLC4,CONW+LY+C-C,-10-MLL,20,MLL
BLC4,CONW+LY+C-C,-10-MLL,20,MLL
BLC4,CONW+LY+C+C+C,-10-MLS,20,MLS

ARSYM,Y,ALL,,0,0
AADD,ALL
ASEL,U,,,ALL

! NEGATIVE PART:
! CONNECT
BLC4,0,-CONL,CONW,CONL
! X SPRING
BLC4,2,-CONL-LX,W,LX
! ANCHOR
BLC4,-6,-CONL-LX-18,18,18
! Y SPRING
BLC4,CONW,-CONL+4*W,LY,W
ARSYM,Y,ALL,,0,0
AADD,ALL
ASEL,U,,,ALL

! POSITIVE PART:
! CONNECT
BLC4,W+CONW-2+MASSL+LY+LY-A-A,-CONL,CONW,CONL
! X SPRING
BLC4,2+W+CONW-2+MASSL+LY+LY-A-A,-CONL-LX,W,LX
! ANCHOR
BLC4,-6+W+CONW-2+MASSL+LY+LY-A-A,-CONL-LX-18,18,18

```

```

! Y, SPRING
BLC4,CONW+W+MASSL+LY-A-A-2,-CONL+4*W,LY,W

ARSYM,Y,ALL,, , ,0,0
AADD,ALL

ASEL,S,,,ALL
! ASEL,S,,,1
! ASEL,S,,,1
! ASEL,S,,,1
! ASEL,S,,,1
! ASEL,S,,,ALL

! ET,1,SHELL63
! KEYOPT,1,1,0
! RMORE, ,

et,1,42,,,3
r,1,2
real,1
! Switch to structural element, PLANE42
! Plane stress with thickness of poly_t

mp,ex,1,169 e3
mp,nuxy,1,0.22
mp,alph,1,29 e-7
! Modulus of elasticity
! Poisson's ratio
! Coefficient of thermal expansion

UIMP,1,EX,,,1.5,e5,
UIMP,1,NUXY,,,
UIMP,1,DENS,,,2333 E-18,

/SOLU
DL,26,,,ALL,0
DL,64,,,ALL,0
DL,71,,,ALL,0
DL,101,,,ALL,0

/PREP7
AMESH,9
AMESH,10
ESIZE,0.1,
AMESH,13,

NSEL,S,,,470
! NSEL,A,,,902
NSEL,A,,,494
! NSEL,A,,,472
ESEL,ALL,ALL
! CP,ALL,ALL
CEINTF,,,ALL

NSEL,S,,,591
! NSEL,A,,,615
! NSEL,A,,,896
ESEL,A,,,473
! CP,ALL,ALL
CEINTF,,,ALL

NSEL,S,,,328
! NSEL,A,,,304
! NSEL,A,,,873
ESEL,A,,,476
! CP,ALL,ALL
CEINTF,,,ALL

NSEL,S,,,207
! NSEL,A,,,183
! NSEL,A,,,879
ESEL,A,,,475
! CP,ALL,ALL
CEINTF,,,ALL

ALLSEL,ALL

/SOLU
*
ANTYPE,2
!
*
MODOPT,SUBSP,6
EQSLV,FRONT
MXPAND,0,,,0
LUMPM,0
PSTRES,0
!
*
MODOPT,SUBSP,6,100,100000,,OFF
RIGID
SUBOPT,8,4,10,0,0,ALL
STATUS,SOLU
SOLVE
/EOF

```